Probing the stability landscape of prestressed stayed columns susceptible to mode interaction

Jiajia Shen[a], Rainer M. J. Groh[a], M. Ahmer Wadee[b], Mark Schenk[a], Alberto Pirrera[a]

[a]*Bristol Composites Institute (BCI), Department of Aerospace Engineering, University of Bristol, Bristol BS8 1TR, UK*
[b]*Department of Civil and Environmental Engineering, Imperial College London, South Kensington Campus, London SW7 2AZ, UK*

Abstract

Prestressed stayed columns are structural systems where the compressive load-carrying capacity is enhanced through pre-tensioned external cable stays. Recent theoretical studies using analytical and nonlinear finite element models have shown that, under certain configurations, this enhancement leads to a sequence of closely spaced bifurcation points beyond the critical one. This undesirable characteristic can give rise to dangerously unstable interactive post-buckling behaviour including 'mode jumping' and 'snaking' phenomena. Even though these highly nonlinear behaviours can be readily modelled using numerical methods, they cannot be verified robustly using traditional quasi-static testing techniques based on force or displacement control at a single point. The current work explores a novel testing concept for potential experimental implementation, from the theoretical and numerical point of view. The concept allows the stability landscape of prestressed stayed columns to be ascertained by controlling the shape of the structure at multiple points. By controlling the mode shape of the structure, it is possible to traverse limit points, path-follow otherwise unstable equilibria, pinpoint bifurcation points and branch-switch between different post-critical segments of the equilibrium manifold. To explore the feasibility of the new testing method, we have created a virtual instantiation of the experiment in the commercial finite element package Abaqus, coupled to a control algorithm that coordinates the movements of the different control points. A number of different stability phenomena that have previously been identified analytically and numerically are reproduced successfully in the virtual test environment. Moreover, a noise sensitivity study is conducted to assess the robustness of the experimental technique proposed herein. The present work lays the foundation for physically assessing the stability landscape of prestressed stayed columns in a more comprehensive way.

Keywords: Virtual testing; Mode jumping; Experimental path-following; Shape control; Newton's method; Branch switch; Measurement noise sensitivity.

*Corresponding author
Email addresses: j.shen@bristol.ac.uk (Jiajia Shen), rainer.groh@bristol.ac.uk (Rainer M. J.

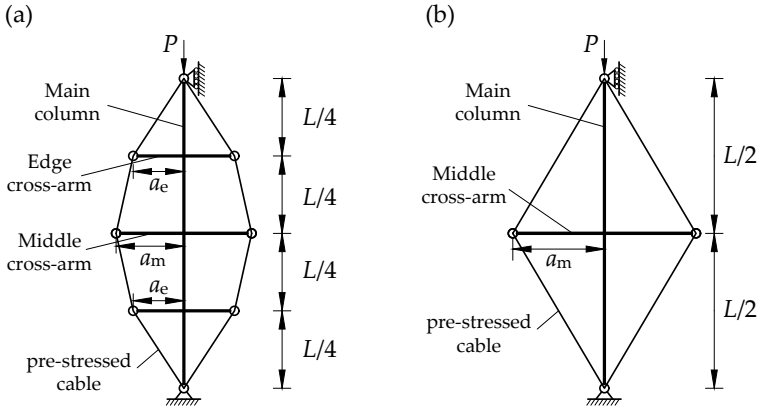

Figure 1: Triple-bay and single-bay prestressed stayed columns with geometric definitions.

1. Introduction

Sustainable design and construction have gradually become mainstream in the structural engineering discipline [1]. Engineers are increasingly expected to exploit the full potential of construction materials designing efficient structural systems that minimise any potentially adverse effect on the environment. Prestressed stayed columns—which comprise a slender main column, a system of crossarms and tensioned cables as shown in Figure 1—offer an innovative, aesthetic and practically significant solution to provide high load-carrying capacity with minimum self-weight [2]. Their easy and fast construction process gives prestressed stayed columns certain advantages over conventional columns [3]. In fact, these advantages have already been exploited in many different structural applications [4, 5]. Owing to their slender structural form, the failure of prestressed stayed columns is generally governed by buckling instabilities. The presence of crossarms and prestress in the cables makes the post-buckling behaviour relatively complex [6–10], particularly for cases where the critical buckling mode is anti-symmetric about the mid-span, and the symmetric and anti-symmetric buckling loads are in close proximity. Highly unstable post-buckling behaviour and nonlinear modal interactions have been identified and predicted using analytical models [8, 11].

However, the availability of equivalent information from experimental tests is comparatively limited [3, 12–14]. Firstly, traditional quasi-static loading techniques based on displacement or force control at one or more points are unable to traverse limit points in the fundamental loading parameter, because the immediate equilibrium beyond limit points is statically unstable, causing the structure to snap to another equilibrium [15]. The dynamic snap makes it difficult to measure the ultimate load accurately. Moreover, the unstable equilibrium solutions between limit points in the stability landscape of prestressed stayed columns are yet to be verified experimentally. The severity of the

Groh), a.wadee@imperial.ac.uk (M. Ahmer Wadee), m.schenk@bristol.ac.uk (Mark Schenk), alberto.pirrera@bristol.ac.uk (Alberto Pirrera)

snap-back beyond limit points is an important indicator of the imperfection sensitivity of slender structures governed by buckling failure [16]. Secondly, in current quasi-static loading techniques, output data are limited to displacements and reaction forces at the main actuation points, and displacements and/or strains at specific points or areas where additional sensors or video gauges are placed. Quantities such as the tangential stiffness matrix, which contains information about the nonlinear behaviour of the test specimen and intrinsic bifurcation properties [17], are not available. Therefore, the implementation of a robust experimental path-following technique that can replicate the functionality of the numerical path-following method is practically significant.

In recent years, many efforts have been made to explore the stability landscape of nonlinear structures experimentally. Virot *et al.* [18] used a 'poker' to perturb an axially loaded cylindrical shell laterally to characterise the stability of the structure under a dominant localised defect. An unstable equilibrium was determined when the reaction force on the poker vanished, because this condition is essentially identical to the *unpoked* shell. However, the poker was not fixed to the shell and, hence, the shell snapped away immediately after reaching the unstable equilibrium.

Van Iderstein & Wiebe [19] adopted extra control points in addition to the main actuation points to stabilise unstable equilibria of a post-buckled beam. These additional control points were also used to approximate an experimental tangential stiffness matrix. Both stable and unstable equilibrium paths were traced using the method. However, owing to the singularity of the experimental tangential stiffness matrix in proximity of the limit point, convergence difficulties arose and manual intervention was necessary for each increment to obtain converged solutions. As a result, the control algorithm could not traverse limit points.

Neville *et al.* [20] developed an experimental method to locate unstable equilibria of nonlinear structures quasi-statically by controlling the structural deformation shape using additional bi-directional probes (so-called 'shape control'). With this method, the unstable segments of the equilibrium path of a transversely-loaded shallow arch were identified experimentally. Neville *et al.* [15] also proposed a 'step-scan' controlling algorithm that is capable of path-following stable and unstable equilibrium paths and traversing limit points without manual intervention. The algorithm was implemented experimentally on a shallow arch loaded by a transverse force. As the step-scan method does not rely on the computation of an experimental Jacobian, it is simple, straightforward and robust. However, useful information from the system's Jacobian, *i.e.* its tangential stiffness matrix, such as measures of the stability of the structure, is not available. Furthermore, without access to a Jacobian it is difficult to scale the method up beyond a single probe or probe pair.

Shen *et al.* [21] subsequently adopted the idea of shape control to formulate an experimental tangential stiffness matrix and developed a control algorithm based on Newton's method to replicate the features of numerical continuation of stationary solutions [22]. A virtual testing environment was implemented in the general purpose Finite Element (FE) package ABAQUS and a proof-of-concept physical experiment on a transversely-loaded shallow circular shallow arch was implemented to validate path-following of stable and unstable

equilibria and traversal of limit points. In particular, excellent comparisons in the converged equilibria and tangential stiffness matrices between the experimental and virtual testing results were observed. Using the virtual testing environment, a FE instantiation of the test setup was created, and the experiment was 'designed' by determining the best combination of control parameters. Shen *el al.* [23] also extended the proposed method to more advanced path-following techniques, including pinpointing critical points, branch switching to alternative equilibrium paths, and path-following along fold lines. Using the virtual testing environment, three pertinent examples—which include design sensitivity plots for shape-adaptive morphing structures, validation of nonlinear FE benchmark models, and non-destructive testing of subcritical (unstable) buckling of thin-walled shells—were presented to demonstrate the effectiveness and potential applications of these advanced functionalities.

The idea of 'probing' a structure using point forces is also being implemented numerically to explore the stability landscape of shell structures [16]. Royer & Pellegrino [24] used probing to investigate the buckling, post-buckling and imperfection sensitivity of ultralight ladder-type coilable space structures. Probing the structure using additional forces to interrogate the stability landscape extends the bifurcation analysis capabilities in existing commercial software packages. For instance, the post-buckling analysis, using static analysis within Abaqus, requires the introduction of geometric or force perturbations. However, perturbations break the symmetry of bifurcations and transforms the bifurcation problem from a branching problem into an imperfect problem of the limit-point variety. With multiple probes and a robust control algorithm, it is possible to achieve the functionality of generalised path-following solvers [22] within commercial FE packages.

The present paper aims to showcase the capability of the experimental path-following method in testing the stability landscape of prestressed stayed columns. The virtual testing environment is created within the commercial FE package Abaqus. In the following sections, firstly, the experimental path-following theory [21] based on shape control [20] and the generalised path-following method [22] are briefly introduced. Then, the implementation of the method and development of the virtual test of the experiment using a finite element model are presented. Subsequently, virtual experimental path-following is conducted on a triple-bay prestressed stayed column and a verification against the nonlinear FE methods is presented. Moreover, a sensitivity study is conducted to assess the robustness of the testing technique in the presence of measurement noise and uncertainties. Finally, conclusions are drawn and future work is outlined.

2. Experimental path-following theory

In this section, a relatively concise but self-contained introduction of shape control and the mathematics of experimental path-following are presented. A more detailed exposition can be found in the authors' earlier work [15, 21, 23].

2.1. Shape control

Shape control is the fundamental building block of the experimental path-following technique [21]. Additional control points—beyond the main actuation points that define the load case imposed on the structure—are added to the test setup. The additional restraint provided by the control points allows for stabilisation against infinitesimal perturbations that would otherwise lead to snaps away from unstable equilibria. Moreover, the additional control points can be used to select different equilibria by deforming the structure until the measured reaction force on all probe points is zero; this condition is equivalent to the case in which the additional probes do not exist. The reader is referred to [20] for more details on the principle of shape control and its experimental implementation.

2.2. Experimental path-following of ordinary (non-critical) points

In the experimental path-following framework [21], the pertinent variables are divided into *state variables*, $\boldsymbol{u} = [\boldsymbol{u}_\mathrm{a}^\top \ \boldsymbol{u}_\mathrm{p}^\top]^\top$, which describe the displacement at the controlling points (main actuation points and probing control points), and *forcing parameters*, $\boldsymbol{\Lambda}$, which control the state. Here, the single parameter system with rigid (displacement-controlled) loading is of interest. The displacement at the actuation points can be expressed as $\boldsymbol{u}_\mathrm{a} = \lambda \hat{\boldsymbol{u}}_\mathrm{a}$, with $\hat{\boldsymbol{u}}_\mathrm{a}$ being an unchanging reference displacement vector. As described in the preceding section on shape control, an equilibrium state corresponds to the vanishing of the reaction forces at all probes (the internal forces at all probing control points):

$$\boldsymbol{R}_\mathrm{p}(\boldsymbol{u}) = \boldsymbol{0}. \tag{1}$$

Here, $\boldsymbol{R}_\mathrm{p}$ is a vector of N_p probe reaction forces and these reaction forces are the functions of all the control point displacements $\boldsymbol{u}$.

Equation (1) can be linearized and written in a partitioned form in terms of the incremental displacements at the main actuation and the probe points:

$$\boldsymbol{K}_\mathrm{T} \Delta \boldsymbol{u} = \begin{bmatrix} \boldsymbol{K}_\mathrm{T}^\mathrm{a} & \boldsymbol{K}_\mathrm{T}^\mathrm{p} \end{bmatrix} \begin{Bmatrix} \Delta \boldsymbol{u}_\mathrm{a} \\ \Delta \boldsymbol{u}_\mathrm{p} \end{Bmatrix} = -\boldsymbol{R}_\mathrm{p}(\boldsymbol{u}), \tag{2}$$

where $\boldsymbol{K}_\mathrm{T}^\mathrm{a} = \partial \boldsymbol{R}_\mathrm{p} / \partial \boldsymbol{u}_\mathrm{a}$ and $\boldsymbol{K}_\mathrm{T}^\mathrm{p} = \partial \boldsymbol{R}_\mathrm{p} / \partial \boldsymbol{u}_\mathrm{p}$ are the tangential stiffness matrix; and the size of $\boldsymbol{K}_\mathrm{T}^\mathrm{a}$ and $\boldsymbol{K}_\mathrm{T}^\mathrm{p}$ are $N_\mathrm{p} \times N_\mathrm{a}$ and $N_\mathrm{p} \times N_\mathrm{p}$, respectively. In the experimental setting, these tangential stiffness matrices can only be approximated using finite difference approximations. Specifically, the ith column of $\boldsymbol{K}_\mathrm{T}$ is given by:

$$\boldsymbol{K}_\mathrm{T}^i = \frac{\boldsymbol{R}_\mathrm{p}(\boldsymbol{u} + \epsilon \left\|\boldsymbol{u}\right\|_2 \boldsymbol{e}_i) - \boldsymbol{R}_\mathrm{p}(\boldsymbol{u})}{\epsilon \left\|\boldsymbol{u}\right\|_2}, \tag{3}$$

where $\boldsymbol{e}_i$ is an $(N \times 1)$-dimensional vector with the ith component being unity and the rest being zero; $\left\|\boldsymbol{u}\right\|_2$ is the L2-norm of the displacement vector, *i.e.* $\left\|\boldsymbol{u}\right\|_2 = (\boldsymbol{u} \cdot \boldsymbol{u})^{1/2}$. As for the experimental procedure, in practice, the ith control point is displaced by a small perturbation $\epsilon \left\|\boldsymbol{u}\right\|_2$, while all other control points remain stationary. Subsequently, the changes in the residual reaction forces at the probe points are measured, *i.e.* $\boldsymbol{R}_\mathrm{p}(\boldsymbol{u} +$

$\epsilon \|\boldsymbol{u}\|_2 \boldsymbol{e}_i) - \boldsymbol{R}_\mathrm{p}(\boldsymbol{u})$. A column of the tangential stiffness matrix can then be computed by dividing the reaction force changes by the small perturbation $\epsilon \|\boldsymbol{u}\|_2$, see Eq. (3). Once one column of the tangential stiffness matrix has been computed, the perturbed control point is moved back to the original position. By repeating this procedure for each control point ($i = 1, 2, \ldots, N$), an 'experimental tangential stiffness matrix' can be assembled. Note that the assembled tangential stiffness matrix $\boldsymbol{K}_\mathrm{T}$ is determined from N_p forces at the probing control points from N incremental displacements at all control points; therefore, the size of the matrix is $N_\mathrm{p} \times N$.

By introducing the forcing parameter λ that describes the applied displacements at the main actuation points, $\boldsymbol{u}_\mathrm{a} = \lambda \hat{\boldsymbol{u}}_\mathrm{a}$, Eq. (2) can be written as:

$$\boldsymbol{K}_\mathrm{T}^\mathrm{a} \hat{\boldsymbol{u}}_\mathrm{a} \Delta\lambda + \boldsymbol{K}_\mathrm{T}^\mathrm{p} \Delta\boldsymbol{u}_\mathrm{p} = -\boldsymbol{R}_\mathrm{p}(\boldsymbol{u}, \lambda). \tag{4}$$

With Eq. (4), we can adopt the predictor–corrector scheme [21] to trace the equilibrium path: (i) determine the predictor, *i.e.* the increment away from a known equilibrium with $\boldsymbol{R}_\mathrm{p} = \boldsymbol{0}$, and (ii) determine the corrector, *i.e.* the iterations towards a new equilibrium with $\boldsymbol{R}_\mathrm{p} \neq \boldsymbol{0}$. Henceforth, a loading step is defined as one step from a known converged equilibrium solution to another, and each loading step is split into predictor and corrector increments. The superscript '1' denotes a predictor increment (the first increment of a loading step) and j denotes any corrector increment.

As for the predictor increment, the incremental displacement factor at the actuation point is prescribed as unity for the first step of a test run. In the subsequent loading steps, the predictor increment is determined by:

$$\Delta\lambda_{j+1}^1 = \left(\frac{n_\mathrm{j}}{n_\mathrm{desired}} \right)^{1/4} \Delta\lambda_j^1, \tag{5}$$

where n_j is the number of iterations required to converge in the preceding step and n_desired is the desired number of iterations. Both virtual and actual experiments reveal that Eq. (5) can lead to a relatively uniform incremental displacement along the solution path, which is good for error control and ensures measurement accuracy.

As for the corrector increment, because there are two unknown quantities in Eq. (4), *i.e.* the incremental displacement factor of the main actuation points $\Delta\lambda$ and the incremental displacement of the probing points $\Delta\boldsymbol{u}_\mathrm{p}$, a linear bordering equation is adopted to solve the linearised equilibrium equation:

$$\Delta\boldsymbol{u}_\mathrm{p}^1 \cdot \Delta\boldsymbol{u}_\mathrm{p}^j + \beta^2 \Delta\lambda^1 \Delta\lambda^j = 0, \tag{6}$$

where the dot represents the scalar product; and β is a scalar quantity that can be used to modify the arc-length definition.

Equations (4) and (6) can now be combined to solve the incremental displacement components at control points ($\Delta\boldsymbol{u}_\mathrm{p}$, $\Delta\lambda$) for the predictor and corrector increments. A bordering algorithm is adopted to solve the equations numerically. Specifically, the in-

crement at the probing control points $\Delta \boldsymbol{u}_{\mathrm{p}}$ are split into two components: (i) $\delta \boldsymbol{u}_{\mathrm{p}}$, the 'tangential' probe displacement arising from the applied displacement at the main actuation points, and (ii) $\mathrm{d}\boldsymbol{u}_{\mathrm{p}}$, a corrector displacement arising from the residual reaction forces at probes $\boldsymbol{R}_{\mathrm{p}}$. Solving Eq. (4) for $\Delta \boldsymbol{u}_{\mathrm{p}}$ in this manner gives:

$$\Delta \boldsymbol{u}_{\mathrm{p}} = \Delta\lambda \delta \boldsymbol{u}_{\mathrm{p}} + \mathrm{d}\boldsymbol{u}_{\mathrm{p}}, \tag{7}$$

where

$$\delta \boldsymbol{u}_{\mathrm{p}} = -\boldsymbol{K}_{\mathrm{T}}^{\mathrm{p}\,-1} \boldsymbol{K}_{\mathrm{T}}^{\mathrm{a}} \hat{\boldsymbol{u}}_{\mathrm{a}} \tag{8a}$$

$$\mathrm{d}\boldsymbol{u}_{\mathrm{p}} = -\boldsymbol{K}_{\mathrm{T}}^{\mathrm{p}\,-1} \boldsymbol{R}_{\mathrm{p}}. \tag{8b}$$

Note that the predictor of the actuation point $\Delta\lambda^1$ is prescribed at the first increment of any load step. For a corrector increment, the appropriate incremental displacement factor $\Delta\lambda^j$ is determined by substituting Eq. (7) into Eq. (6):

$$\Delta\lambda^j = -\frac{\Delta \boldsymbol{u}_{\mathrm{p}}^1 \cdot \mathrm{d}\boldsymbol{u}_{\mathrm{p}}^j}{\Delta \boldsymbol{u}_{\mathrm{p}}^1 \cdot \delta \boldsymbol{u}_{\mathrm{p}}^j + \beta^2 \Delta\lambda^1}. \tag{9}$$

Once the incremental displacement factor at the main actuation controlling points $\Delta\lambda^j$ ($j = 1, 2, \cdots$) is determined, the predictor or corrector incremental displacement at the main actuation and probing control points can be determined using $\Delta \boldsymbol{u}_{\mathrm{a}} = \Delta\lambda \hat{\boldsymbol{u}}_{\mathrm{a}}$ and Eq. (7), respectively. During experimentation in practice, all the control points remain stationary when solving these equations. When the right combination of $\Delta \boldsymbol{u}_{\mathrm{a}}$ and $\Delta \boldsymbol{u}_{\mathrm{p}}$ has been determined by the control algorithm, the main actuation and the probing control points can be moved in concert in one single step.

Moreover, to traverse limit points, the sign of the predictor $\Delta\lambda^1$, *i.e.* the direction of the incremental displacement of the actuation point(s), needs to be controlled. This is achieved by checking the sign of the scalar product of the total displacement increment of the probes (predictor plus correctors) in the previous load step, $\Delta \boldsymbol{u}_{\mathrm{p}}^{\mathrm{prev}}$, and the current 'tangential' probe displacement predictor $\delta \boldsymbol{u}_{\mathrm{p}}^1$:

$$\begin{aligned} &\textbf{if } \Delta \boldsymbol{u}_{\mathrm{p}}^{\mathrm{prev}} \cdot \delta \boldsymbol{u}_{\mathrm{p}}^1 > 0 \\ &\quad \Delta\lambda^1 = \|\Delta\lambda^1\| \\ &\textbf{else} \\ &\quad \Delta\lambda^1 = -\|\Delta\lambda^1\|, \end{aligned} \tag{10}$$

where the magnitude of $\Delta\lambda^1$ is determined from Eq. (5). The algorithm for experimental path-following is summarised in Figure Appendix A.1.

2.3. Critical point pinpointing and branch switching

Besides determining the predictor and corrector during path following, the experimental tangential stiffness also provides information about the stability of the equilibria and

the intrinsic bifurcation properties of the tested structure from the eigenvalues and the corresponding eigenvectors of $\boldsymbol{K}_{\mathrm{T}}^{\mathrm{p}}$. Specifically, the structure is (locally) stable if all the eigenvalues are positive; the structure is (locally) unstable if one of the eigenvalues is negative; and neutrally stable if one eigenvalue is zero while all others are positive. Moreover, when the number of negative eigenvalues between two consecutive converged equilibria changes, there must exist a critical point between these two converged equilibria. The eigenvector corresponding to the zero eigenvalue can help determine the type of critical point, *i.e.* whether it is a limit point or a branching bifurcation point [17, 22]. If it is the latter, the eigenvector can further be used to switch the branch onto the bifurcated path.

2.3.1. Pinpointing critical points

Currently, the location of critical points is pinpointed within a certain numerical tolerance using the direct method [22]. This method uses a bordering equation to describe the singularity of $\boldsymbol{K}_{\mathrm{T}}^{\mathrm{p}}$ and is solved using Newton's method. In the experimental setting, the direct method is more efficient than the indirect method [17, 25], which is based on bisection to zero on the critical point.

In the experimental control system, the eigenvalue problem is first solved independently, and equilibrium is then sought in a second step while keeping the eigenvalue μ and eigenvector $\boldsymbol{\phi}$ constant. In the second step, the equilibrium equations are augmented with the scalar singularity condition:

$$\mathbf{G}(\boldsymbol{u}_{\mathrm{p}}, \lambda) \equiv \begin{Bmatrix} \boldsymbol{R}_{\mathrm{p}}(\boldsymbol{u}_{\mathrm{p}}, \lambda) \\ \mu(\boldsymbol{u}_{\mathrm{p}}, \lambda) \end{Bmatrix} = \mathbf{0} \tag{11}$$

to find an equilibrium state that satisfies the singularity constraint. By linearising Eq. (11), a singular point $(\boldsymbol{u}_{\mathrm{p}}^{*}, \lambda^{*})$ is calculated via Newton's method using the iteration matrix:

$$\begin{bmatrix} \boldsymbol{K}_{\mathrm{T}}^{\mathrm{p}} & \boldsymbol{K}_{\mathrm{T}}^{\mathrm{a}} \hat{\boldsymbol{u}}_{\mathrm{a}} \\ \frac{\partial \mu}{\partial \boldsymbol{u}_{\mathrm{p}}}^{\top} & \frac{\partial \mu}{\partial \lambda} \end{bmatrix} \begin{Bmatrix} \Delta \boldsymbol{u}_{\mathrm{p}} \\ \Delta \lambda \end{Bmatrix} = - \begin{Bmatrix} \boldsymbol{R}_{\mathrm{p}}(\boldsymbol{u}_{\mathrm{p}}, \lambda) \\ \mu(\boldsymbol{u}_{\mathrm{p}}, \lambda) \end{Bmatrix}. \tag{12}$$

The first row of Eq. (12) features the linearised equilibrium condition previously introduced, and the tangential stiffness matrix, which is readily computed by finite differences from the probe force measurements. The second row features derivatives of the bordering equation, and hence derivatives of the singularity condition. These quantities can also be determined based on the finite difference approximations [23]:

$$\frac{\partial \mu}{\partial \boldsymbol{u}_{\mathrm{p}}} \approx \frac{\boldsymbol{R}_{\mathrm{p}}(\boldsymbol{u}_{\mathrm{p}} + \gamma \boldsymbol{\phi}, \boldsymbol{u}_{\mathrm{a}}) - 2\boldsymbol{R}_{\mathrm{p}}(\boldsymbol{u}_{\mathrm{p}}, \boldsymbol{u}_{\mathrm{a}}) + \boldsymbol{R}_{\mathrm{p}}(\boldsymbol{u}_{\mathrm{p}} - \gamma \boldsymbol{\phi}, \boldsymbol{u}_{\mathrm{a}})}{\gamma^2}, \tag{13a}$$

$$\frac{\partial \mu}{\partial \lambda} \approx \frac{\boldsymbol{\phi}^{\top}}{\epsilon} \left(\frac{\boldsymbol{R}_{\mathrm{p}}(\boldsymbol{u}_{\mathrm{p}} + \gamma \boldsymbol{\phi}, \boldsymbol{u}_{\mathrm{a}} + \epsilon \hat{\boldsymbol{u}}_{\mathrm{a}}) - \boldsymbol{R}_{\mathrm{p}}(\boldsymbol{u}_{\mathrm{p}}, \boldsymbol{u}_{\mathrm{a}} + \epsilon \hat{\boldsymbol{u}}_{\mathrm{a}})}{\gamma} - \boldsymbol{K}_{\mathrm{T}}^{\mathrm{p}}(\boldsymbol{u}_{\mathrm{p}}, \boldsymbol{u}_{\mathrm{a}}) \boldsymbol{\phi} \right), \tag{13b}$$

where the perturbation scale factors γ and ϵ should satisfy the following deformation com-

patibility relationship:

$$\gamma = \frac{\left\| \boldsymbol{K}_{\mathrm{T}}^{\mathrm{p}\,-1} \boldsymbol{K}_{\mathrm{T}}^{\mathrm{a}} \hat{\boldsymbol{u}}_{\mathrm{a}} \epsilon \right\|}{\|\phi\|}. \tag{14}$$

The governing equation for pin-pointing critical points, Eq. (12), is solved in the typical manner using a partitioning procedure. The incremental factor $\Delta\lambda$ in the displacement at the actuation point(s) gives:

$$\Delta\lambda = -\frac{\mu + \mu_{,\boldsymbol{u}}^{\top} \mathrm{d}\boldsymbol{u}_{\mathrm{p}}}{\mu_{,\lambda} + \mu_{,\boldsymbol{u}}^{\top} \delta\boldsymbol{u}_{\mathrm{p}}}, \tag{15}$$

where $\delta\boldsymbol{u}_{\mathrm{p}}$ and $\mathrm{d}\boldsymbol{u}_{\mathrm{p}}$ are computed using Eqs. (8a) and (8b), respectively; and the partial derivatives of μ with respect to $\boldsymbol{u}_{\mathrm{p}}$ and λ are then computed using Eqs. (13a) and (13b). When $\Delta\lambda$ is obtained, the incremental displacement in the controlling points can be determined accordingly. The controlling algorithm for pinpointing the critical points is summarised in Figure Appendix A.2.

2.3.2. Branch switching

When the bifurcation point $\boldsymbol{u}^* = (\boldsymbol{u}_{\mathrm{a}}^*, \boldsymbol{u}_{\mathrm{p}}^*)$ has been pinpointed, the branch-switching procedure can be implemented. At the bifurcation point, $\boldsymbol{K}_{\mathrm{T}}^{\mathrm{p}} \boldsymbol{\phi} = \boldsymbol{0}$ with $\boldsymbol{\phi}$ being the critical eigenvector corresponding to a zero eigenvalue. Therefore, the predictor for the first step onto the new branch is adopted as follows:

$$\Delta\boldsymbol{u}_{\mathrm{a,bs}}^{1} = \boldsymbol{0}, \quad \Delta\boldsymbol{u}_{\mathrm{p,bs}}^{1} = \zeta \frac{\boldsymbol{\phi}}{\|\boldsymbol{\phi}\|_2}, \tag{16}$$

where the magnitude of the scaling factor ζ is determined from:

$$\zeta = \pm \frac{\left\|\boldsymbol{u}_{\mathrm{p}}^*\right\|_2}{\rho}, \tag{17}$$

with the sign of ζ controlling the direction of path-following along the bifurcated path, and ρ being a problem-specific constant in the range of 1–100. It should be noted that in the case where $\boldsymbol{u}_{\mathrm{p}}^*$ is zero, $\boldsymbol{u}_{\mathrm{a}}$ is adopted in Eq. (17) instead and ρ is determined using trial and error. Once the predictor is defined, the corrector subroutine presented in Figure Appendix A.1 is adopted to solve the converged equilibrium state on the branched path.

3. Virtual Testing (VT) Environment and Finite Element model development

3.1. Virtual testing environment

The experimental path-following procedure is implemented in the commercial FE package ABAQUS as a virtual instantiation of the actual experiment, as shown in Figure 2. The displacement control at the probes and actuation point is achieved by setting the displacement boundary conditions with specific values, which mimics the role of actuators in experiments. A general static solver (no possibility to traverse limit points numerically)

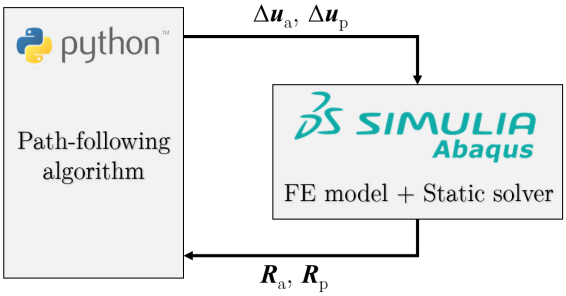

Figure 2: Virtual testing environment. The details of the path-following algorithm can be found in Sections 2.2 and 2.3.

is adopted to obtain the reaction force at the probes and actuation points, which mimics the reaction force measurement system in an experiment. The individual control points are then synchronised using a control system based on the methodology outlined in the preceding section using PYTHON scripts. The implementation details of the virtual testing environment can found in [21].

3.2. Development of Finite Element Model

In ABAQUS, the column and the crossarms are modelled with Timoshenko beam elements with linear interpolation formulations B21, and the stays are modelled with 2-node truss elements T2D2 [26]. In particular, the 'no compression' option within ABAQUS is enabled in the stay elements to ensure that they can carry tensile stresses only. The prestress in the stays is modelled as an *initial condition*. The main column is simply supported at both ends; the crossarms are rigidly connected to the main column; and the stays are pinned to the ends of the main column and the crossarms, which reflects that the stays can slide through frictionless supports freely. The modelling techniques have been verified by analytical methods [11] and adopted by other researchers on similar problems [27].

For verification purposes, a geometrically nonlinear analysis using the static nonlinear solver Riks [28] within ABAQUS using the same FE model is conducted. Currently, there is no facility implemented in the Riks solver of ABAQUS to pinpoint critical points or branch switch. Therefore, initial perturbations in the geometry are introduced in the FE model to transform the bifurcation problem into a continuous one. Specifically, both symmetric and anti-symmetric linear buckling modes are introduced in order to reproduce the mode jump. The imperfection scaling factors for the anti-symmetric and symmetric modes are 0.01 and 0.04, respectively. These values are sufficiently small to ensure that the response can mimic the perfect system as far as possible and mode interaction can be triggered, the latter manifesting itself by exhibiting symmetry breaking in the equilibrium path and the deflected shape.

Table 1: Material and geometric properties of the prestressed stayed columns.

Young's modulus of the main column and crossarms	$E_{\mathrm{c}} = E_{\mathrm{a}} = 201$ kN/mm^2
Young's modulus of the stays	$E_{\mathrm{s}} = 202$ kN/mm^2
Yield stress of the main column	$f_{\mathrm{y}} = 355$ N/mm^2
Outside diameter of the main column and crossarms	$\phi_{\mathrm{co}} = \phi_{\mathrm{ao}} = 38.1$ mm
Inside diameter of the main column and crossarms	$\phi_{\mathrm{ci}} = \phi_{\mathrm{ai}} = 26.3$ mm
Diameter of the stays for triple-bay column	$\phi_{\mathrm{s3}} = 2.5$ mm
Length of the main column for triple-bay column	$L = 5080$ mm
Length of the edge crossarm for triple-bay column	$a_{\mathrm{e}} = 508$ mm
Length of the middle crossarm for triple-bay column	$a_{\mathrm{m3}} = 406.4$ mm

4. Virtual testing results and verification: ideal case

Virtual testing is assumed to be ideal, *i.e.* geometric imperfections in the column as well as noise and uncertainties in the measurement and actuator systems are excluded. A triple-bay prestressed stayed column under axial compression is considered, as shown in Figure 1. The material and geometric properties of the stayed column are presented in Table 1. The prestress level in the cable stays is 400 MPa.

The column is loaded by displacement control at the actuation point on the top sliding support, while three independent probes are introduced at the joints of the crossarms and the main column to control the shape of the prestressed stayed column by providing horizontal restraint, as shown in Figure 3(a, b). The probes are free to rotate and move vertically in order to avoid reaction moments and vertical reaction forces that would disturb the equilibrium path. Note that it is also assumed that the stiffness of the probe system is significantly larger than the tested column so that no additional bifurcation points would be introduced due to the elastic restraints. The effects of elastic restraints from the probe system on the experimental path-following is left for future work.

Referring to Eq. (3), the size of the experimental tangential stiffness matrix $\boldsymbol{K}_{\mathrm{T}}^{\mathrm{p}}$ is 3×3. With the probe layout, both symmetric and anti-symmetric modes as well as their combinations can be controlled and captured, see Figure 3(c, d). To measure the contribution of the symmetric and anti-symmetric mode contribution, the following quantities are defined:

$$Q_1 = u_{\mathrm{p2}}, \quad Q_2 = \frac{u_{\mathrm{p1}} - u_{\mathrm{p3}}}{2}, \tag{18}$$

where $u_{\mathrm{p}i}$ (with $i = \{1,\ 2,\ 3\}$) are the horizontal displacements of probes, as shown in Figure 3(b).

4.1. Fundamental path

Figure 4(a) presents the converged equilibria with the number of negative eigenvalues of the experimental tangential stiffness matrix $\boldsymbol{K}_{\mathrm{T}}^{\mathrm{P}}$ on the fundamental path. The critical bifurcation point can be pinpointed and the corresponding eigenmode can also be obtained.

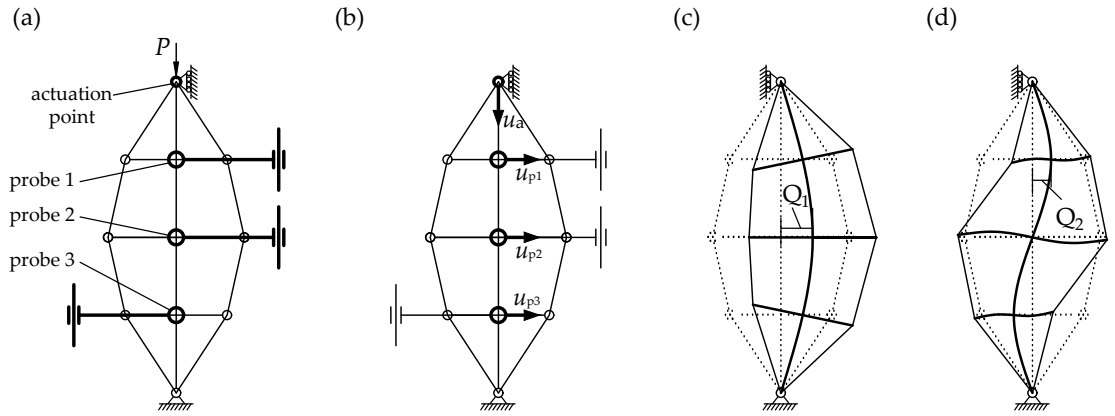

Figure 3: (a) Probe layout for the triple-bay prestressed stayed column for shape control. Note that the probes allow rotations and vertical displacements to prevent reaction moments and vertical reaction forces that would perturb the equilibrium path. (b) Displacement at the probes and actuation point. (c, d) Symmetric and anti-symmetric buckling modes, where Q_1 and Q_2 are defined in Eq. (18).

In particular, the three elements in the eigenmode are partitioned into the horizontal displacement components of the three probes. The critical buckling mode is anti-symmetric. Moreover, owing to the stabilisation restraint from the probes, we can trace along the fundamental path beyond the critical bifurcation point and obtain the higher-order bifurcation paths. The critical eigenmodes at bifurcation points BP2 and BP3 are both symmetric. As noted in [21], the least number of independent probes introduced should be equal to the maximum number of negative eigenvalues of $\boldsymbol{K}_{\mathrm{T}}$ in the path investigated. Currently, the probes will lose control authority over the column at the fourth bifurcation point on the fundamental path. Additional probes are required for the path to follow further along the fundamental path.

It is worth noting that the buckling loads and the corresponding critical eigenmodes are almost the same as those from the linear buckling analysis using ABAQUS, as shown in Table 2. This is reasonable since the load–end-shortening response of the system is practically linear in this range; see the inset in Figure 4. The greater discrepancy of the third bifurcation point with respect to the first buckling point between the two methods stems from the fact that the experimental path-following method employs a nonlinear critical point solver, whereas conventional linear buckling analysis is based on linearisation about the unloaded state. To illustrate the corresponding critical eigenmodes at the bifurcation points, the first three linear buckling modes are presented in Figure 4(b–d).

4.2. Interactive buckling path

Since the fundamental path beyond the first bifurcation point B1 is unstable, branch switching is performed at the first bifurcation point using the technique described in Section 2.3.2 with the scale factor $\rho = 1$. The converged equilibria and the deformed configuration of the column from virtual testing are presented in Figure 5. The equilibria on

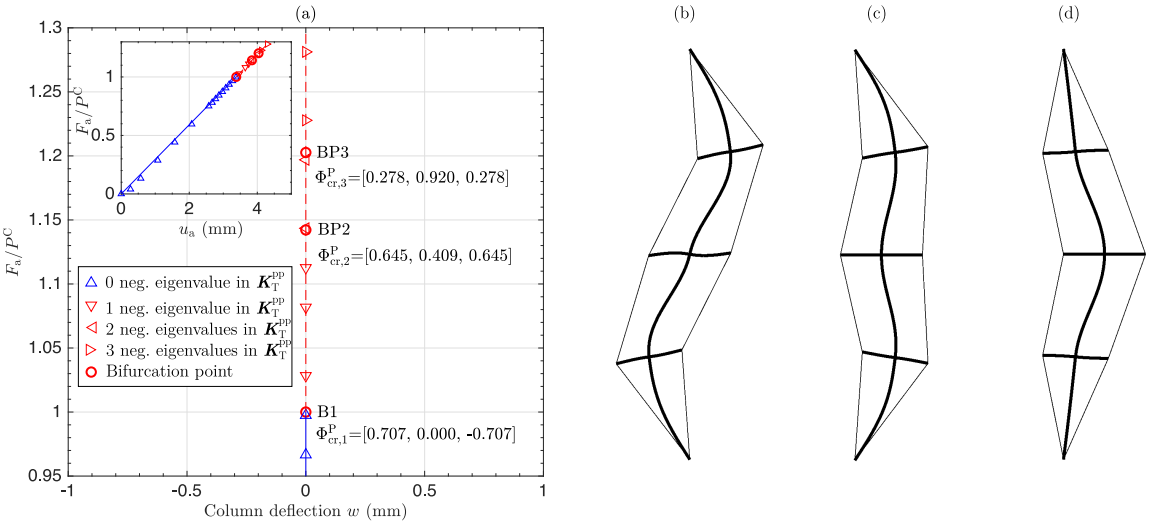

Figure 4: (a) Virtual testing results of the prestressed stayed column on the fundamental path. The main figure and the inset present the load versus out-of-plane deflection and load versus end-shortening relationships, respectively; P^{C} is the compression load at the first bifurcation point B_1, *i.e.* the critical buckling load. Blue solid and red dashed lines represent the stable and unstable paths. Triangles represent the converged equilibrium states; BP_i and $\Phi^{\mathrm{P}}_{\mathrm{cr},i}$ (with $i = \{1, 2, 3\}$) represent the bifurcation point and the corresponding critical eigenvector. (b–d) Approximated eigenmodes of the main column at the bifurcation points B1, BP2, BP3 from linear buckling analysis using ABAQUS. The deformation has been scaled by a factor of 500 to aid visualisation.

Table 2: Comparison of the bifurcation loads and critical eigenmodes on the fundamental path from the experimental path-following (VT) and conventional linear buckling analysis (LBA). Note that the elements in the eigenmodes correspond to the horizontal displacement of the three probes.

		1st		2nd		3rd	
		VT	LBA	VT	LBA	VT	LBA
Buckling load (kN)		85.842	85.824	98.048	97.954	103.236	103.417
Eigenmode	u_{p1}	0.707	0.707	0.645	0.641	0.278	0.269
	u_{p2}	0.000	0.000	0.409	0.422	0.920	0.925
	u_{p3}	-0.707	-0.707	0.645	0.641	0.278	0.269

the secondary branch (B1→B2) are stable with the number of negative eigenvalues in $\boldsymbol{K}_{\mathrm{T}}^{\mathrm{p}}$ being zero and the column deforming in an anti-symmetric mode.

With the increase of the anti-symmetric deformation mode amplitude Q_2, a secondary bifurcation point is reached with the critical eigenvector $\Phi_{\mathrm{cr,B2}} = [0.732, 0.549, 0.404]$. Beyond B2, the anti-symmetric mode becomes unstable, *i.e.* there is at least one negative eigenvalue in $\boldsymbol{K}_{\mathrm{T}}^{\mathrm{p}}$, the details of which will be discussed in Section 4.3. Branch switching at B2 with the critical eigenvector $\Phi_{\mathrm{cr,B2}}$ and $\rho = 10$ breaks the anti-symmetry and the symmetric mode component Q_1 begins to increase, as shown in Figure 5(b). The triggering of mode interaction is accompanied by a snap-back in the load-end-shortening relationship and a drop in the load-carrying capacity. Under conventional displacement controlled loading techniques, the column would undergo a dynamic load reduction when B2 is reached. These results suggest that with the current testing technique based on shape control this highly unstable segment of equilibrium path can be traced.

As for the structural deformation profile, one cable on the more compressed side becomes slack, *i.e.* the internal force is zero, see LP1 in Figure 5(c). The column regains stability as the continuation proceeds, *i.e.* all the eigenvalues of $\boldsymbol{K}_{\mathrm{T}}^{\mathrm{p}}$ become positive. There is a kink on the stable path, which corresponds to the slackening of another cable segment, see Figure 5(c). The column remains stable until the second limit point LP2 is reached. In the range between SP and LP2, both the anti-symmetric component Q_1 and symmetric component Q_2 increase. At the limit point LP2, three cable segments on the more compressed side are slack. This is followed by a sharp snap-back in the $F_{\mathrm{a}}/P^{\mathrm{C}}$ versus u_{a} relationship, where the tension force in the last tensioned cable on the more compressed side decreases and the anti-symmetric deformation component Q_2 decreases to zero. When the bifurcation point B_3 is reached, all four cable segments on the more compressed side of the column become slack. The anti-symmetric deformation mode component is practically zero and the column deforms in a symmetric mode, as shown in Figure 5(b, c). The complete process from B1 to B3 is known as 'mode jump' [11, 29], which accords well with the observed behaviour from analytical modelling results [11]. Beyond B3, the number of negative eigenvalues in $\boldsymbol{K}_{\mathrm{T}}^{\mathrm{p}}$ is zero and the prestressed stayed column is henceforth stable under displacement controlled loading.

Even though no imperfections are introduced in the virtual testing environment and the noise in the measurement system is excluded, potential sources of error still exist. The main sources of error come from the non-zero residual reaction force tolerance at the probes and the numerical errors during the computation within the controlling algorithm. Currently, the residual reaction force tolerance at each probe $R_{\mathrm{p,tol}}$ is set as 0.5 N. The maximum residual reaction force within the probes at the converged equilibria are presented in Figure 6. In the range where the column deforms in a purely anti-symmetric mode or symmetric mode, the symmetric component and anti-symmetric component should be theoretically zero, respectively. However, owing to numerical errors, they are not exactly zero. For instance, the prestressed stayed column should deform in a purely anti-symmetric mode on the secondary path B1–B2 and the contribution of the symmetric mode Q_1 should be zero. However, it was observed that Q_1 is not precisely zero at the converged equilibria. The break in anti-symmetry also leads to the difference in the residual reaction forces at

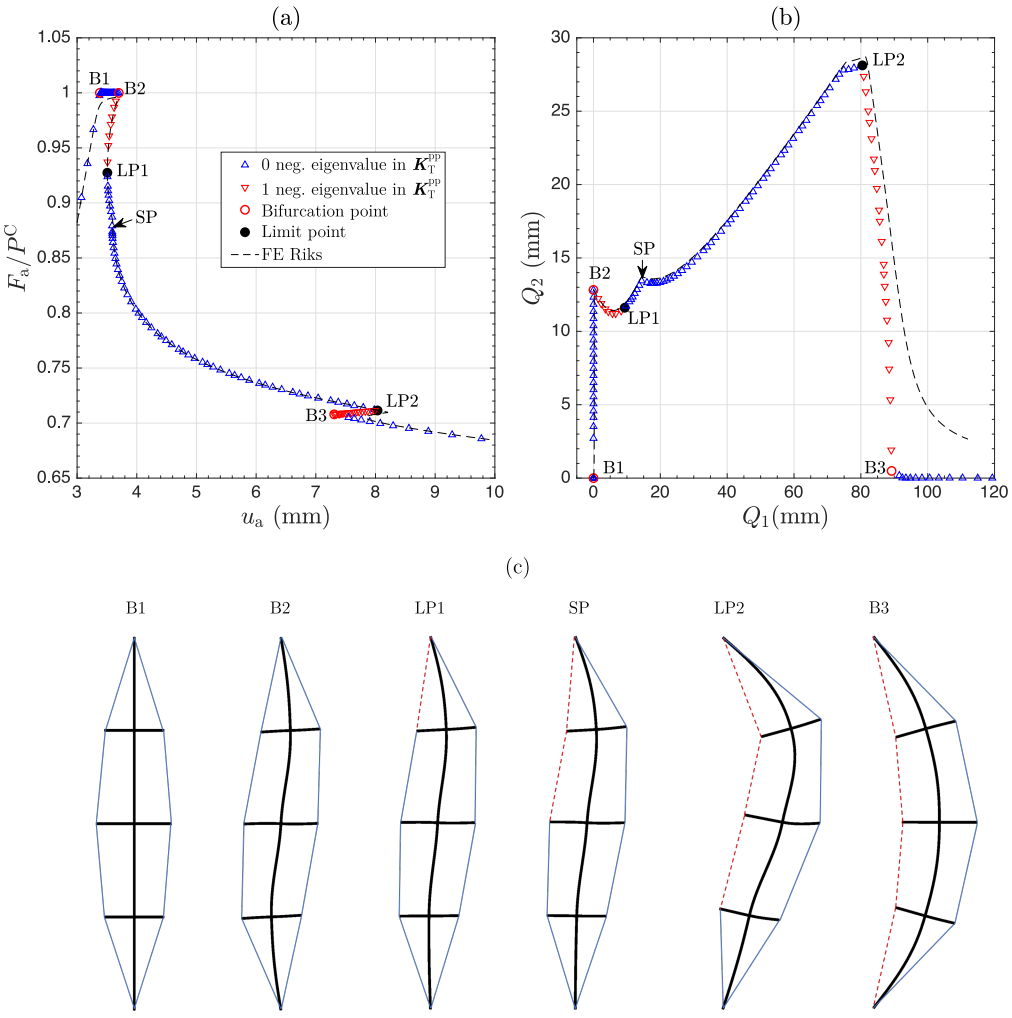

Figure 5: Virtual testing results of triple-bay prestressed stayed column under pure compression and the corresponding structural deformation profiles. (a–b) are as described in Figure 4(a). Solid circles represent limit points. Q_1 and Q_2 are defined by Eq. (18). The deformation profiles in (c) are those equilibria with the same labels in (a–b). The red dashed and blue solid lines represent the cable is slack and under tension, respectively. The deformation has been scaled by a factor of 10 to aid visualisation.

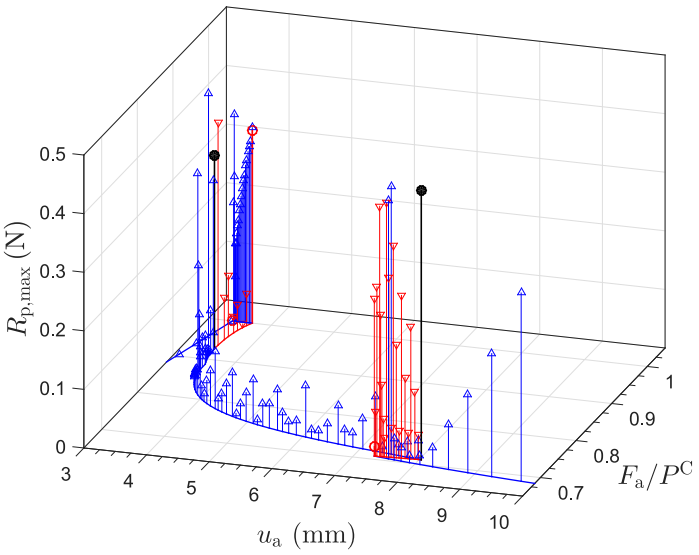

Figure 6: The maximum residual reaction force at probes $R_{\mathrm{p,max}}$ at the converged equilibria. Note that the convergence condition for the residual reaction force is 0.5 N; details are as described in Figure 5(a).

probes 1 and 3, which otherwise should be identical. Further errors are introduced and accumulate during the corrector steps. Note that this type of error can be mitigated by adopting a smaller $R_{\mathrm{p,tol}}$. All these factors imply that the system cannot fully go back to the symmetric mode at the bifurcation point B3, *i.e.* Q2 is not exactly zero. However, it should be noted that Q_2 approximates to zero when the continuation process goes further. Therefore, it may be concluded that the current system is robust under numerical errors and the bespoke level of residual reaction force tolerance.

For verification purposes, nonlinear solutions from the FE Riks solver within Abaqus are compared with the virtual testing results. Good correlation is observed in terms of the converged equilibria. However, as noted in Section 3.2, geometric perturbations are introduced in the verification FE model in order to bypass the discontinuity at the bifurcation points and trigger the mode interaction. Owing to the high sensitivity to imperfections of the nonlinear system, the introduced imperfections break the symmetry of the system. The prestressed stayed column cannot fully jump back to the symmetric mode in the advanced post-buckling range, as shown by the dashed curve in Figure 5(b).

4.3. Equilibrium manifold

Owing to the stabilisation restraint provided by the probes, the unstable equilibria with multiple negative eigenvalues in $\boldsymbol{K}_{\mathrm{T}}^{\mathrm{p}}$ can be accessed such that a more complete equilibrium manifold is obtained. This can facilitate the understanding of the intrinsic bifurcation properties of the prestressed stayed column. Figure 7 presents the converged equilibria on the fundamental path, and also on secondary and tertiary branches from the virtual testing environment, plotted in terms of the end-shortening u_{a} versus the normalised

reaction force F_a/P^C at the main actuation point of the prestressed stayed column. Red triangles with different directions represent unstable equilibria with at least one negative eigenvalue in $\boldsymbol{K}_T^p$. Hollow and solid circles represent bifurcation points and limit points, respectively. The interactive buckling path presented in Figure 5(a) is plotted using solid curves with blue and red segments representing stable and unstable equilibria, respectively.

As noted in Section 4.1, the fundamental path (path 1) is unstable beyond the first bifurcation point B1. Path 2 emanating from the primary bifurcation point B1 on the fundamental path is stable until the bifurcation point B2 is reached. On path 2, the prestressed stayed column deforms in an anti-symmetric mode, as shown in Figure 7(b), and reaching the bifurcation point is accompanied by the slackening of a pair of cable segments. Even though there is no snap-back on path 2 and the actuation point increases monotonically, the equilibria are unstable, *i.e.* the column would snap-down to path 5 upon the removal of the probes. It should also be noted that the number of slack cable segments does not increase even in the advanced post-buckling range, as shown by the second column deformation profile in Figure 7(b).

Path 3 emanating from BP2 is unstable until it reaches the bifurcation point B3, where it intersects with path 5. There are a pair of limit points on the path, *i.e.* LP3 and LP4. Reaching LP3 triggers snap-back and the slackening of a pair of cables on the more compressed side near the supports, as observed in the second column deformation profile in Figure 7(c). Note that the number of negative eigenvalues in $\boldsymbol{K}_T^p$ increases from one to two after traversing limit point LP3. When LP4 is reached, the number of negative eigenvalues in $\boldsymbol{K}_T^p$ decreases to one. This is also accompanied by the slackening of all four cable segments on the more compressed side, as observed in the third column deformation profile in Figure 7(c).

Path 4 emanating from BP3 is unstable with the number of negative eigenvalues in $\boldsymbol{K}_T^p$ being 2. Unlike paths 2 and 3, there is no snap-back in the load–end-shortening relationship upon the slackening of cables. No bifurcation point is detected. There are also four slack cable segments in the advanced post-buckling range, as shown in Figure 7(d).

As discussed in Section 4.2, path 5 is the tertiary branch emanating from the secondary branch 2 and connecting paths 2 and 3. It corresponds to the mode jump from the purely anti-symmetric mode to the symmetric mode.

For verification purposes, nonlinear solutions from the FE Riks solver within Abaqus are superimposed in Figure 7(a) as dashed curves. The perturbation amplitude in the geometry of the FE models is 0.01 mm with the corresponding critical buckling mode at each bifurcation point, as presented in Figure 5(b–d). Paths 2–4 show good correlation with the nonlinear solution results. It should be noted that the deformation profiles of the column on paths 3 and 4 are symmetric. To solve for path 4, we adopt a small perturbation size, since a relatively large perturbation size (for instance, 0.1 mm) would lead the column onto path 3 instead.

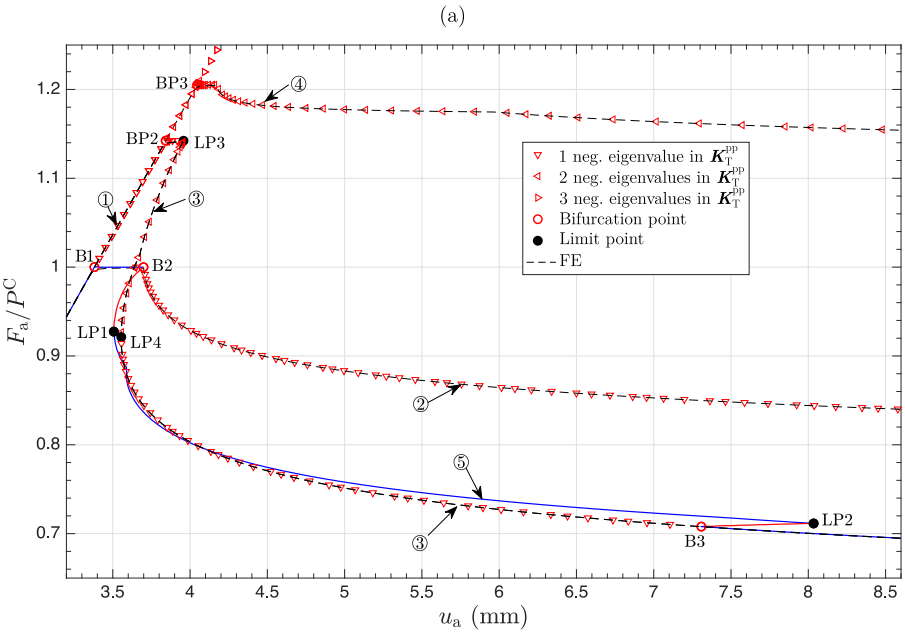

(b) Path 2 (c) Path 3 (d) Path 4

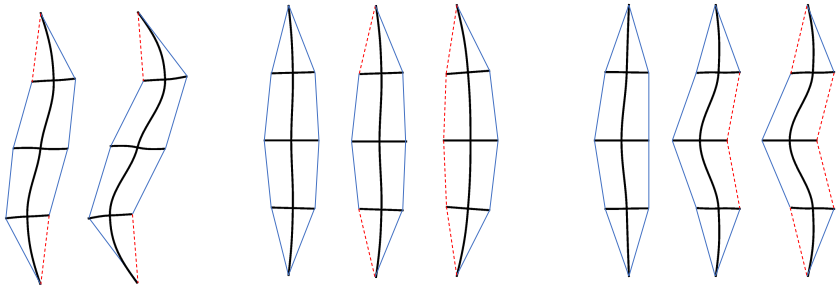

u_{a} (mm)	4.284	8.038	3.916	3.953	3.556	4.144	5.136	5.840
$F_{\mathrm{a}}/P^{\mathrm{C}}$	0.909	0.844	1.143	1.141	0.914	1.205	1.177	1.175

Figure 7: (a) Virtual experimental path-following results for the equilibrium manifold of the prestressed stayed column with three independent probes. Numerical results obtained using the standard Riks solver in ABAQUS are superimposed as dashed curves with the path numbering system shown in circles. Path 1 corresponds to the fundamental path where the column remains straight; paths 2–4 are secondary paths bifurcating from the fundamental path; path 5 is the tertiary branch emanating from the secondary branch 2 and connecting paths 2 and 3, which corresponds to the interactive buckling response discussed in Section 4.2. (b–d) Deformation of the prestressed stayed column at converged equilibria on paths 2–4. The deformation has been scaled by a factor of 10 to aid visualisation.

5. Noise sensitivity analysis

In the preceding section, the noise and measurement uncertainty stemming from sensors, actuators and the data collection system were not considered. However, these effects cannot be avoided in actual physical experiments. The virtual testing environment provides the possibility to explore these effects and design an experimental set-up to minimise the effect of noise. The effects of noise and uncertainties in displacement and reaction forces are modelled by perturbing the displacements and reaction forces [21]:

$$\boldsymbol{u}_{\text{real}} = \boldsymbol{u}_{\text{ideal}} + \Delta\boldsymbol{u}_{\text{err}}, \quad \boldsymbol{R}_{\text{p,real}} = \boldsymbol{R}_{\text{p,ideal}} + \Delta\boldsymbol{R}_{\text{p,err}}, \tag{19}$$

where subscript 'real' represents the 'measured' data used in the controlling algorithm; subscript 'ideal' represents idealised control signals or zero-noise measurements; and subscript 'err' represents the noise or error. Specifically, for the displacements, noise is added before the *restart analysis* for any loading increment to mimic 'real' displacements, whereas the 'ideal' value is adopted in the rest of the controlling algorithm. Note that all the loading steps are enclosed using double rectangles in the control algorithms presented in Appendix A. For the reaction forces, noise is augmented to from the static solver and this 'real' value is then adopted in the controlling algorithm. The perturbation in the displacement $\Delta\boldsymbol{u}_{\text{err}}$ and force $\boldsymbol{R}_{\text{p,err}}$ can be assumed to follow a normal (Gaussian) distribution and modelled using the function NUMPY.RANDOM.NORMAL in PYTHON [21].

Before conducting virtual testing, the effects of noise on the path-following controlling algorithm are analysed. As for the effects on the experimental tangential stiffness approximation, virtual testing on a shallow arch [21] has shown that $\boldsymbol{K}_{\text{T}}$ obtained using the finite difference approximation based on two data points, see Eq. (3), is sensitive to measurement noise. A recent physical testing on a shallow arch [21] has demonstrated that a least-square regression using the whole force–displacement data of the perturbation loading history can diminish the effects of noise and the approximated $\boldsymbol{K}_{\text{T}}$ shows good comparisons with the perfect case along the equilibrium path. Therefore, the effects of noise are excluded in the perturbation loading step to approximate $\boldsymbol{K}_{\text{T}}$ herein. Moreover, it is assumed that this also applies to the approximation of the second-order directional derivatives, see Eqs. (13a) and (13b). For this to be achieved, the controlling points are required to be moved in a synchronised approach during the perturbation step. Therefore, the current study focuses on the effects of noise on path-following of ordinary (non-critical) points.

The convergence condition requires the residual reaction force at each probe to fall below the tolerance level $R_{\text{p,tol}}$. Referring to Eq. (4), the errors introduced in the reaction forces in the predictor/corrector step stemming from displacement noise can be approximated as:

$$\Delta\boldsymbol{R}_{\text{p,err}} \approx \boldsymbol{K}_{\text{T}}\Delta\boldsymbol{u}_{\text{err}}. \tag{20}$$

For the probe i, Eq. (20) can be written as:

$$\Delta R^{i}_{\text{p,err}} \approx K^{i}_{\text{pa}}\Delta u_{\text{a,err}} + \sum_{j=1}^{n_{\text{p}}} K^{ij}_{\text{pp}}\Delta u^{j}_{\text{p,err}}, \tag{21}$$

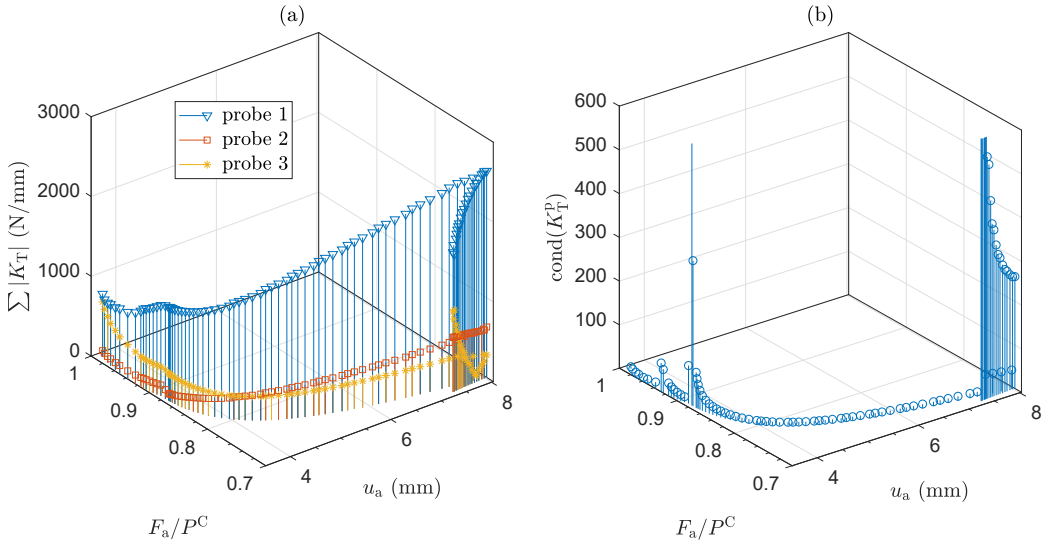

Figure 8: (a) Summation of the absolute value of a specific row of the tangential stiffness matrix for the equilibria on path 5 (interactive buckling path) presented in Figure 7(a). The magnitude is a measure of sensitivity of the reaction force at probes to the displacement noises. (b) The condition number of the tangential stiffness matrix at the equilibria on path 5. The magnitude is a measure of the sensitivity of $\boldsymbol{K}_{\mathrm{T}}^{\mathrm{p}}$ to noises and numerical errors.

where n_{p} is the number of probe control points. If $\left|\Delta R_{\mathrm{p,err}}^{j}\right| > R_{\mathrm{p,tol}}$, convergence difficulty may arise due to noise. In order to obtain converged solutions under these circumstances, we have to increase $R_{\mathrm{p,tol}}$ or use actuators with better control fidelity, *i.e.* to decrease $\Delta u_{\mathrm{a,err}}$ and $\Delta u_{\mathrm{p,err}}$.

Equation (21) also provides a criterion to determine the residual reaction tolerance based on the fidelity of measurement sensors and actuators, and vice versa. For the current case, it is assumed that the noise magnitude in the displacement actuators are the same, *i.e.* $\Delta u_{\mathrm{a,err}} = \Delta u_{\mathrm{p,err}}^{j}$ $(j = 1, 2, \cdots, n_{\mathrm{p}})$. Based on the $\boldsymbol{K}_{\mathrm{T}}$ at converged equilibria in the ideal case (no noise) from virtual testing, we can estimate the lower limit of the residual reaction force tolerance for the ith probe by summing-up the absolute value of the ith row of $\boldsymbol{K}_{\mathrm{T}}$:

$$R_{\mathrm{p,tol}}^{i} \geq \Delta u_{\mathrm{err}} \left(\left| K_{\mathrm{pa}}^{i} \right| + \sum_{j=1}^{n_{\mathrm{p}}} \left| K_{\mathrm{p}}^{ij} \right| \right). \tag{22}$$

Figure 8(a) presents the variation of $\left|K_{\mathrm{pa}}^{i}\right| + \sum_{j=1}^{n_{\mathrm{p}}} \left|K_{\mathrm{p}}^{ij}\right|$ along the interactive buckling path (path 5 in Figure 7(a)) of the prestressed stayed column. It can be seen that three probes exhibit different sensitivity to displacement noise and the sensitivity also varies along the equilibrium path. For better accuracy, different $R_{\mathrm{p,tol}}$ values could be adopted at different equilibria and for different probes based on Eq. (22). Currently, the same value of $R_{\mathrm{p,tol}}^{i}$ $(i = 1, 2, 3)$ along the interactive buckling path is adopted for all probes.

5.1. Sensitivity to residual reaction force tolerance level

In the displacement-controlled system, the effects of unrelated (white) noise in the force measurement can be diminished by taking multiple measurements and adopting the average value [21]. The focus of the current research on noise sensitivity of force measurements is on the effects of correlated (system) noise. The effects are considered by conducting a parametric analysis on the residual reaction force tolerance levels. Moreover, the residual reaction force tolerance determines the degree to which the controlling algorithm forces the tested structure converge to the 'true' solution, *i.e.* the 'accuracy' of the virtual testing result. The sensitivity to this value also provides reference for the sensitivity to uncertainty in the probe force measurement as well as the robustness of the controlling algorithm.

Figure 9 presents the virtual testing results of different reaction force tolerance levels. Note that the parameters in the controlling algorithm are the same as those adopted in Figure 5. Moreover, for comparison purposes, the virtual testing results with $R_{\mathrm{p,tol}} = 0.5\,\mathrm{N}$ and the numerical solution using the FE nonlinear solver are superimposed as coloured solid curves and black dashed curves, respectively. In all four cases presented, the controlling algorithm can trace the interactive buckling path without any convergence difficulties and the converged equilibria generally show good correlation with the virtual testing results with $R_{\mathrm{p,tol}} = 0.5\,\mathrm{N}$ and the nonlinear numerical solutions. The residual reaction forces at the probes for most converged states are much smaller than the tolerance, as presented in Figure 10. Moreover, as noted in previous work on shallow arches [21], the effects of residual reaction force tolerance levels are also affected by the maximum incremental displacement step size. If the incremental step size is small, convergence can be reached within the predictor step and the corresponding residual reaction force may also be much smaller than the tolerance value.

However, the relatively large residual reaction at the converged equilibria breaks the perfect pitchfork of the equilibrium path, *i.e.* the embedded symmetry/anti-symmetry of the prestressed stayed column, and transforms the perfect pitchfork bifurcation into an imperfect one of the limit-point variety. As shown in the Q_1–Q_2 relationship in Figure 9, the column goes back to the symmetric mode automatically without branch switching. With the increase of $R_{\mathrm{p,tol}}$, the results become closer to the numerical solution of the FE model with geometric perturbations using the Riks solver. Generally, it may be concluded that the current controlling algorithm is insensitive to $R_{\mathrm{p,tol}}$ and robust for path-following of ordinary equilibrium states in nonlinear structures.

5.2. Sensitivity to displacement uncertainties

Compared with the force measurement, the uncertainties in the displacement actuators cannot be easily controlled or diminished because the displacement is applied only once at all controlling points in each loading increment. Referring to Eq. (22), the sensitivity analysis is conducted in a deterministic manner, *i.e.* a fixed magnitude of noise Δu_{err} is adopted for all control points during a specific virtual testing run. The sign of Δu_{err} for each control point is determined to ensure that the largest $\Delta R^{i}_{\mathrm{p,err}}$ can be obtained using Eq. (21).

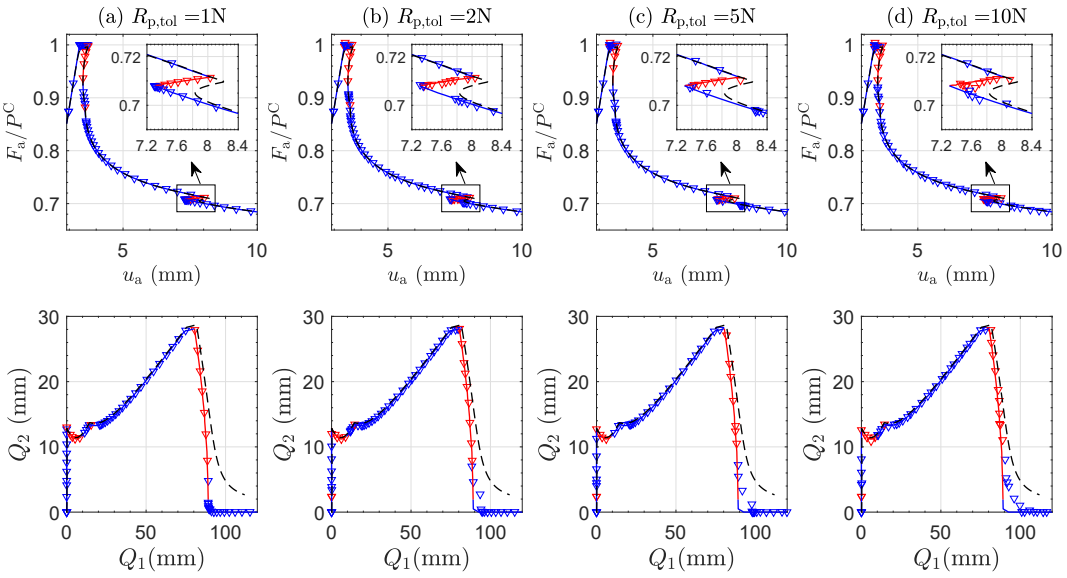

Figure 9: Effects of residual reaction force tolerance on the virtual testing results; the graphs are as described in Figure 5.

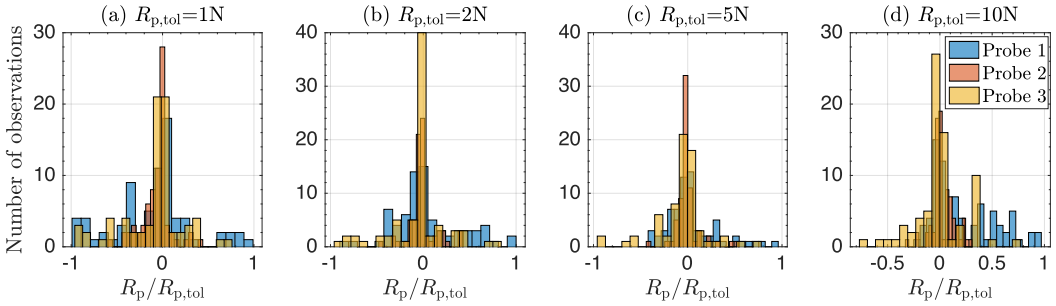

Figure 10: Distribution of the magnitude of the residual reaction force at the converged equilibria for different residual reaction force tolerance levels; the corresponding converged equilibria are presented in Figure 9.

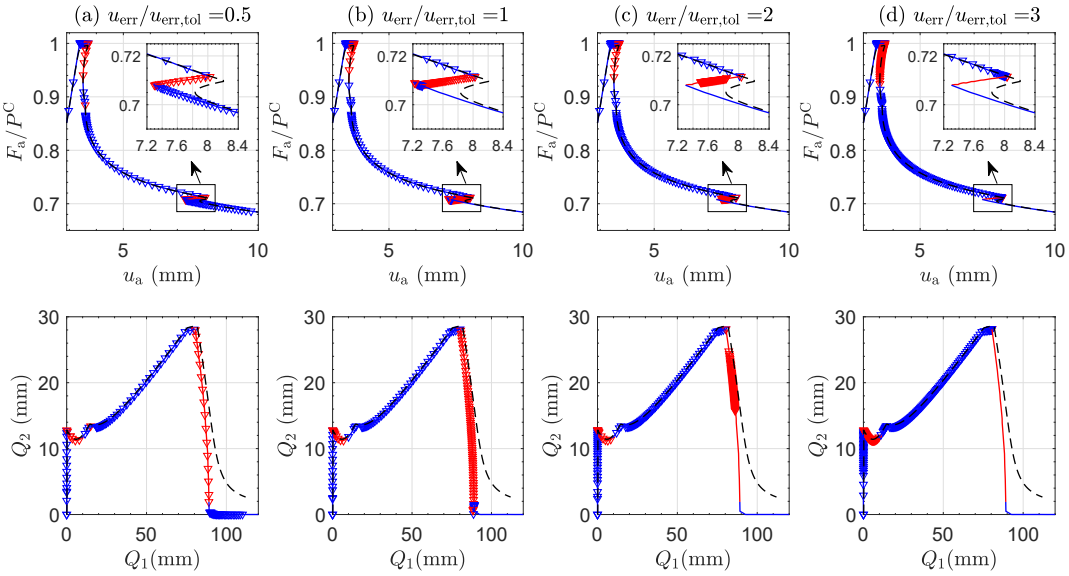

Figure 11: Effects of displacement noise on the virtual testing results. The tolerance of the residual reaction force at the probes is 0.5 N; $u_{\mathrm{err,tol}}$ is the maximum displacement error approximated using Eq. (21) with $R_{\mathrm{p,tol}} = 0.5\,\mathrm{N}$. The graphs are as described in Figure 5.

Figure 11 presents the converged equilibria with different displacement noise levels. All the parameters in the controlling algorithm are the same as those adopted in Figure 5 in Section 4.2. The displacement noise levels are normalised with respect to the tolerance error $\Delta u_{\mathrm{err,tol}}$ determined using Eq. (21) with the residual reaction force tolerance $R_{\mathrm{p,tol}} = 0.5\,\mathrm{N}$. The converged equilibria show good correlation with the case that has no displacement noise. Similar to the force noise, the introduced displacement noise breaks the embedded structural symmetry/anti-symmetry and transforms the bifurcation problem into a continuous one. The controlling algorithm can trace the interactive buckling path without manually imposed branch switching. With the increase of Δu_{err}, more iterations are required to reach convergence. Since the controlling algorithm is free to adapt the incremental displacement at controlling points for each loading step based on the convergence rate, the incremental step size decreases as Δu_{err} increases. The small incremental step size in turn makes the effects of displacement noise more significant, causing the algorithm to get stuck.

Since the convergence difficulty stems from the stringent residual reaction force tolerance, the problem can be remedied by adopting a relatively large $R_{\mathrm{p,tol}}$. Figure 12(a) presents the virtual testing results for a prestressed stayed column with $R_{\mathrm{p,tol}} = 3\,\mathrm{N}$, while the other parameters and the displacement noise remain the same as in Figure 11(d). Accordingly, $u_{\mathrm{err}}/u_{\mathrm{err,tol}} = 0.5$ in this case. The incremental step size becomes larger and the full interactive buckling path can be traced without any convergence difficulties. However, as noted in Section 5.1, the large residual reaction force tolerance introduces imperfections and breaks the pitchfork, which makes the results deviate from the perfect equilibria.

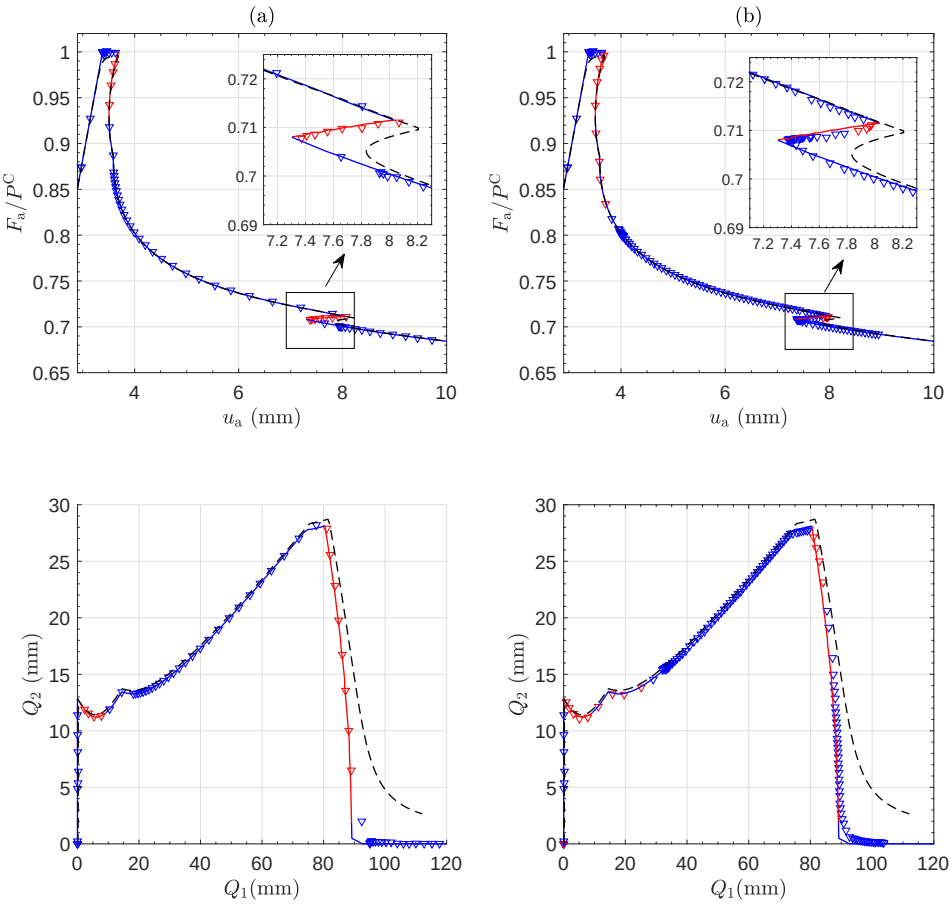

Figure 12: The virtual testing results of the prestressed column with $R_{p,tol} = 3\,N$. Note that the absolute displacement noise magnitude in the actuators are the same as that in Figure 11(d) while $u_{err}/u_{err,tol} = 0.5$ in the current case. The direction of the perturbation displacement to approximate the tangential stiffness matrix in (a) is the same as the direction of Q_1, while the direction is opposite in (b). The other details of the graph are the same as described in Figure 5.

It should be noted that the convergence difficulty does not arise at the equilibrium configuration with the largest $\left|K_{\mathrm{pa}}^{i}\right|+\sum_{j=1}^{n_{\mathrm{p}}}\left|K_{\mathrm{p}}^{ij}\right|$, as predicted by Eq. (22). This is attributed to the fact that the actual tangential stiffness matrix during the corrector increments is different from the initial tangential stiffness matrix obtained in the last converged equilibrium state. Moreover, the residual reaction forces due to noise may be cancelled out by the 'ideal' non-zero residual reaction force at converged equilibria. However, considering the simplicity, Eq. (22) provides a relatively reliable relationship between the residual reaction force tolerance and the requirement for the fidelity of the displacement actuator.

6. Discussion

6.1. Functionality of probes

From the preceding examples, the probes do not only provide restraints to stabilise the structure and control the structural shape, but also play the role of 'sensors' that monitor the real-time structural stiffness properties through the experimental tangential stiffness matrix. Specifically, the tangential stiffness matrix contains information about (i) how to coordinate each individual probe to reach the converged state such that $R_{\mathrm{p}}<R_{\mathrm{p,tol}}$; (ii) the stability of the converged equilibria from the number of negative eigenvalues in $\boldsymbol{K}_{\mathrm{T}}^{\mathrm{p}}$; and (iii) the bifurcation properties at critical points and the corresponding eigenvector. Probes also serve as 'actuators' to switch the structure onto the secondary or tertiary paths based on the critical eigenvector of the tangential stiffness matrix at bifurcation points. However, the reliability of these functionalities is based on the assumption that the probe system is fully rigid. Any elastic interaction between the probe system and the tested structure would lead to inaccurate experimental results that do not reflect the actual nonlinear behaviour of test structures.

6.2. Implications for physical experimental design: noise sensitivity and probing perturbation direction

As shown in Section 5, the controlling algorithm reveals to be robust within a reasonable size of displacement and force measurement noise. Equation (22) provides a simple criterion to select the residual reaction force tolerance based on the fidelity of actuators and *vice versa*. Generally, the structure of tangential stiffness matrix components with large magnitudes may have a very stringent requirement on the fidelity of the actuator so as to obtain converged equilibria that are close to the 'perfect' solution. In some cases, it is probably beyond the capability of most existing actuators. Under these circumstances, a scaled structural model [30] with a smaller magnitude in $\boldsymbol{K}_{\mathrm{T}}$ may need to be adopted, rather than a full-scale model, to ensure that the required fidelity of the displacement actuator or force sensors are within the scope of accessible equipment.

Currently, the effects of noise are excluded in the approximation of the tangential stiffness matrix. However, errors may be introduced at the limit points of the probe displacement or critical points of the equilibrium path, which may correspond to sign changes of the components in $\boldsymbol{K}_{\mathrm{T}}^{\mathrm{pa}}$ and the non-diagonal terms in $\boldsymbol{K}_{\mathrm{T}}^{\mathrm{p}}$, as shown in Figure 13. In

these cases, there is a limit point in the reaction force–perturbation displacement relationship. Least squares regression using the whole data set would always lead to inaccurate approximations of the tangential stiffness components. This, in turn, may lead to slow convergence (fine incremental step size) or even divergence of the algorithm, which has been observed in previous work on the experimental path-following of shallow arches [21]. In particular, the effects may be even more significant in the range where the condition number of $\boldsymbol{K}_{\mathrm{T}}^{\mathrm{p}}$ is large. Herein, the problem is remedied by the restarting facility in the controlling algorithm with a reduced predictor step size. In real testing scenarios, a similar functionality may be difficult to implement due to the hysteresis in the test system. A self-corrector scheme may have to be implemented to modify the tangential stiffness components based on the residual reaction force variation during the iteration process, when they are close to zero. A similar functionality has been implemented for one probe case experimentally [21].

Since the slackening of cable leads to a sharp drop in the stiffness, the approximated tangential stiffness matrix $\boldsymbol{K}_{\mathrm{T}}$ is affected by the perturbation size and direction, particularly in the range where the cable tensile force is close to zero. Figure 12(b) presents the virtual testing results with an opposing perturbation direction to that in Figure 12(a). Even though the full equilibrium path with the opposite perturbation direction can be obtained, the approximated tangential stiffness matrix does not reflect the actual structural stiffness properties. Specifically, the number of negative eigenvalues in $\boldsymbol{K}_{\mathrm{T}}^{\mathrm{p}}$ is 1 on some stable equilibria immediately after the first limit point on the interactive buckling path and zero in the unstable snap-back range beyond the second limit point. The inaccurate approximation of $\boldsymbol{K}_{\mathrm{T}}$ also leads to an incorrect predictor, which is naturally followed by more corrector iteration steps and a very fine incremental step-size to reach the converged equilibria. Therefore, a sensitivity study on the perturbation direction should be conducted in the virtual testing environment to determine the best scheme for perturbation direction.

6.3. Advantage and weakness as an advanced numerical path-following solver

The critical point locating and branch-switching capability of the virtual testing environment extends the functionality of ABAQUS beyond bifurcation analysis based on perturbations so that the stability landscape of a perfect structure, without geometric perturbations, can be obtained. Currently, post-buckling analysis using static analysis within ABAQUS requires the analyst to be aware of possible bifurcation points and buckling modes in advance and choose a reasonable perturbation size as well as a selection of appropriate buckling modes, and such a procedure requires *ad hoc* user intervention. An inappropriate choice of perturbation size or eigenmodes may lead to an inaccurate depiction of the nonlinear behaviour and, more importantly, potentially unsafe strength prediction.

Owing to the discretisation of the finite element method, modal information is not straightforward to extract; a post-processing step is required to acquire useful information with clear physical meaning. With the current methodology, the probes can be analogous to the discrete generalised coordinates in the Rayleigh-Ritz method, which can provide direct and quantitative insight into the bifurcation properties of the nonlinear structure.

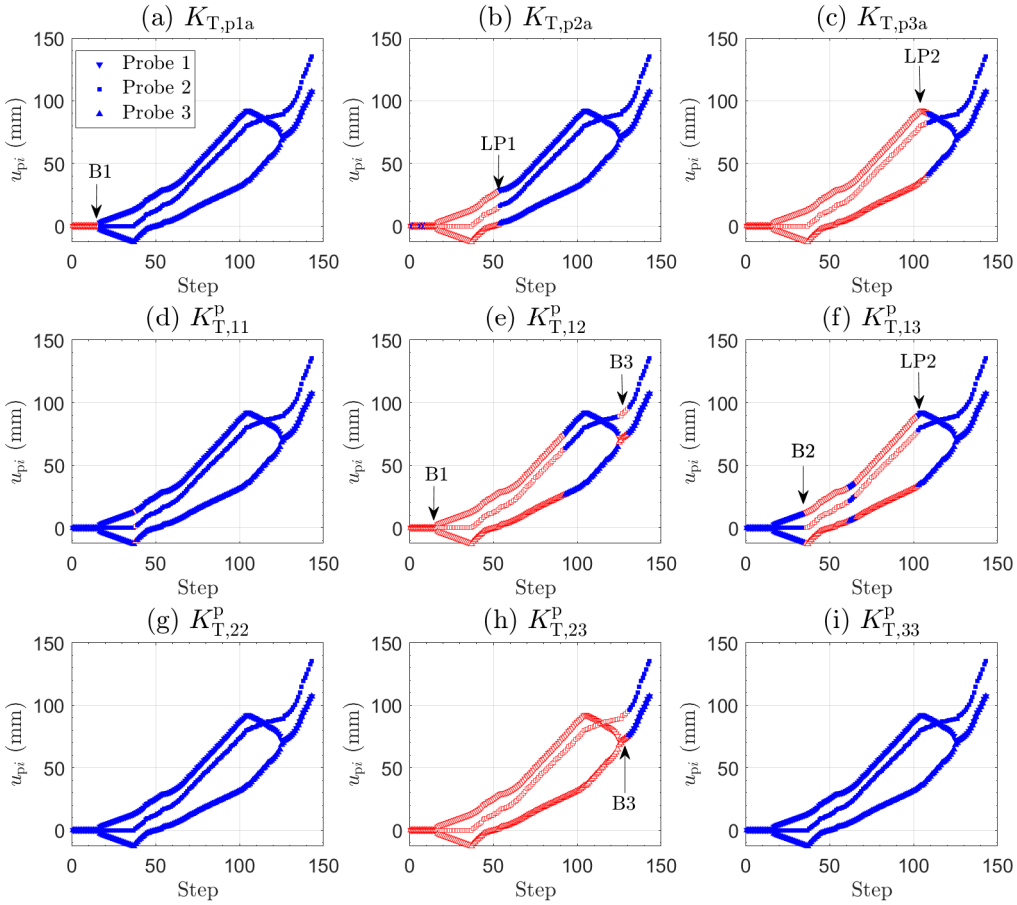

Figure 13: Probe displacement variation and the sign of tangential stiffness matrix components at converged equilibria from the virtual testing results presented in Figure 5. Note that blue solid and red hollow shapes represent positive and negative signs respectively.

Analytical methods are an excellent tool to reveal the underlying aforementioned properties with good computational efficiency [11]. However, it may become cumbersome when the structural geometry or loading cases are complex. A slight change in the structural topology or loading case may require development of a new model from scratch. Developing a reasonable and accurate analytical model also requires physical insight from the modeller of the nonlinear problem. Owing to the excellent pre-processor in ABAQUS, the virtual testing environment can unveil the intrinsic bifurcation properties of much more complex structural geometries with minimal extra effort. Moreover, the accuracy of the analytical model largely depends on the choice of shape functions. An increase in the degrees of freedom would greatly increase the complexity of any nonlinear analytical model, while the accuracy of the virtual testing results can be ensured by choosing a reasonable mesh scheme and a residual reaction force tolerance level.

However, the success of the proposed method primarily depends on shape control, *i.e.* the probe layout scheme. To choose an optimal probe layout scheme, the critical eigenvectors at the critical points encountered during the loading history are required [21]. For a nonlinear structure with complex bifurcational properties, this can only be achieved by conducting a general path-following analysis [22]. Moreover, as noted in Section 3.1, the experimental path-following process in the current virtual testing environment is essentially a sequential solution method. Every loading increment in the experiment requires the creation of an individual job alongside a restarting and stopping process, which consumes the majority of the computation time. Therefore, the efficiency of the proposed path-following technique is relatively low, compared with the embedded Riks solver within ABAQUS. There exists an efficient and promising approach by employing the UAMP subroutine [26], the user-defined subroutine in ABAQUS. With the subroutine, the boundary conditions are modified increment-by-increment as the simulation executes, *i.e.* the analysis would not be stopped during the process. However, this development is left for future work.

7. Conclusions

A virtual implementation of an experimental path-following technique on a three-bay prestressed stayed column susceptible to mode interaction has been presented using the general purpose FE package ABAQUS. Three additional probes are introduced to control the shape of the column so that the column can be stabilised when unstable. The experimental tangential stiffness matrix is approximated by perturbing the column at the three control points and well-established numerical methods based on Newton's method [22] are adopted as the control algorithm to trace both stable and unstable equilibrium paths, locate critical points and switch branches at bifurcations.

Virtual testing was conducted in the ideal scenario (no measurement noise and geometrically perfect) and scenarios with different levels of force and displacement noise. In the ideal case, the intrinsic bifurcation properties of the prestressed stayed column were revealed through the equilibrium manifold and highly unstable snap-back behaviour was captured, which is otherwise inaccessible using conventionally displacement or force con-

trolled testing techniques. Mode jumps from anti-symmetric modes to symmetric modes were reproduced and it was identified that the 'mode jump' is essentially linked to slackening in the stays. The results were verified using the arclength solver within ABAQUS, which largely showed excellent correlations. The ability to trace the unstable equilibrium segments can provide a better understanding of the failure mechanism, which may otherwise be veiled using traditional displacement- or force-controlled loading. More importantly, the severity of the snap-back can also be used as an indicator of the imperfection sensitivity of tested prestressed stayed columns. The functionality to explore the entire bifurcation landscape provides a way to identify potentially isolated stable equilibria, which could be exploited to improve the load-carrying capacity of tested columns using 'modal nudging' [31].

Virtual testing considering noise from the displacement actuators and the residual reaction force measurement was conducted to verify the robustness of the proposed method. The addition of noise breaks the perfect pitchfork bifurcation and transforms the bifurcation problem into a continuous one. As for the residual reaction force tolerance ($R_{\mathrm{p,tol}}$) sensitivity, the residual reaction forces in the probes have been revealed to be much smaller than the tolerance at most converged equilibria. The converged equilibra deviated more from the 'ideal' solution with the increase of $R_{\mathrm{p,tol}}$ but no convergence problems arose. Noise in the displacement actuators led to convergence difficulty when the resultant reaction forces at the probes is of the same order of magnitude as $R_{\mathrm{p,tol}}$. The problem can be remedied by adopting a relatively large $R_{\mathrm{p,tol}}$. A simple relationship between the residual reaction force tolerance and the displacement actuator noise level is provided, which can help experimentalists choose a reasonable $R_{\mathrm{p,tol}}$ from the fidelity of the displacement actuators and *vice versa*.

The present method provides a robust and efficient tool to unveil the intrinsic bifurcational structure of nonlinear structural systems within the general purpose FE package ABAQUS. This can be used as a better verification tool than the current nonlinear Riks solver within ABAQUS for systems that have a sequence of bifurcation instabilities. More importantly, it can provide guidance on the experimental design for the path-following of nonlinear structures, *i.e.* the choice of structural geometry, probe layout scheme, the fidelity of the actuators and the choice of controlling parameters in the controlling algorithm. Further work will focus on the implementation of the proposed testing technique on an actual physical test. The ultimate aim is to develop a general-purpose physical loading and probing control system such that complex nonlinear behaviour of prestressed stayed columns can be captured in physical experiments.

Acknowledgments

This work was funded by the Royal Academy of Engineering and the Engineering and Physical Sciences Research Council (EPSRC) under their Research Fellowship schemes [Grant no. \ RF\201718\17178 for Rainer M. J. Groh and EP/M013170/1 for Alberto Pirrera]. The support of all funders is gratefully acknowledged.

Appendix A. Control algorithms for experimental path-following

Figures Appendix A.1 and Appendix A.2 depict algorithms for experimental path-following of ordinary (non-critical) points and for locating critical points as presented in [21, 23].

References

[1] C. J. Kibert, Sustainable construction: green building design and delivery, John Wiley & Sons, 2016.

[2] E. Belenya, Prestressed load-bearing metal structures, Moscow: Mir Publishers, 1977.

[3] R. R. De Araujo, S. A. L. De Andrade, P. C. G. d. S. Vellasco, J. G. S. Da Silva, L. R. O. De Lima, Experimental and numerical assessment of stayed steel columns, J. Constr. Steel. Res. 64 (2008) 1020–1029.

[4] J. Yu, Nonlinear stability of prestressed stayed columns with multiple crossarm systems, Ph.D. thesis, Imperial College London (2017).

[5] S. Krishnan, Cable-stayed columns and their applications in building structures, J. Build. Eng. 27 (2020) 100984.

[6] D. Saito, M. A. Wadee, Post-buckling behaviour of prestressed steel stayed columns, Eng. Struct. 30 (5) (2008) 1224–1239.

[7] D. Saito, M. A. Wadee, Numerical studies of interactive buckling in prestressed steel stayed columns, Eng. Struct. 31 (2) (2009) 432–443.

[8] M. A. Wadee, L. Gardner, T. A. Hunt, Buckling mode interaction in prestressed stayed columns, Proc. Inst. Civ. Eng. Struct. Build. 166 (2013) 403–412.

[9] P. Li, M. A. Wadee, J. Yu, M. Wu, Stability of prestressed stayed steel columns with a three branch crossarm system, J. Constr. Steel. Res. 122 (2016) 274–291.

[10] K. Wu, M. A. Wadee, L. Gardner, Interactive buckling in prestressed stayed beam-columns, Int. J. Mech. Sci. 174 (2020) 105479.

[11] J. Yu, M. A. Wadee, Mode interaction in triple-bay prestressed stayed columns, Int. J. Non-Linear Mech. 88 (2017) 47–66.

[12] A. I. Osofero, M. A. Wadee, L. Gardner, Experimental study of critical and post-buckling behaviour of prestressed steel stayed columns, J. Constr. Steel. Res. 79 (2012) 226–241.

[13] M. Serra, A. Shahbazian, L. Simões da Silva, L. Marques, C. Rebelo, P. C. G. d. S. Vellasco, A full scale experimental study of prestressed stayed columns, Eng. Struct. 100 (2015) 490–510.

[14] A. Köllner, M. Todt, G. Ganzosch, C. Völlmecke, Experimental and numerical investigation on pre-stressed lattice structures, Thin-Walled Struct. 145 (2019) 106396.

[15] R. M. Neville, R. M. J. Groh, A. Pirrera, M. Schenk, Beyond the fold: experimentally traversing limit points in nonlinear structures, Proc. Roy. Soc. A: Math., Phys. Eng. Sci. 476 (2020) 20190576.

[16] R. Groh, A. Pirrera, On the role of localizations in buckling of axially compressed cylinders, Proc. Roy. Soc. A: Math., Phys. Eng. Sci. 475 (2224) (2019) 20190006.

[17] M. A. Crisfield, J. J. Remmers, C. V. Verhoosel, et al., Nonlinear finite element analysis of solids and structures, John Wiley & Sons, 2012.

[18] E. Virot, T. Kreilos, T. M. Schneider, S. M. Rubinstein, Stability landscape of shell buckling, Phys. Rev. Lett. 119 (2017) 224101.

[19] T. van Iderstein, R. Wiebe, Experimental path following of unstable static equilibria for snap-through buckling, in: G. Kerschen (Ed.), Nonlinear Dynamics, Volume 1, Springer International Publishing, 2018, pp. 17–22.

[20] R. M. Neville, R. M. Groh, A. Pirrera, M. Schenk, Shape control for experimental continuation, Phys. Rev. Lett. 120 (25) (2018) 254101.

[21] J. Shen, R. M. J. Groh, M. Schenk, A. Pirrera, Experimental Path-Following of Equilibria Using Newton's Method. Part I: Theory, Modelling, Experiments, Int. J. Solids Struct. 210 (2021) 203–223.

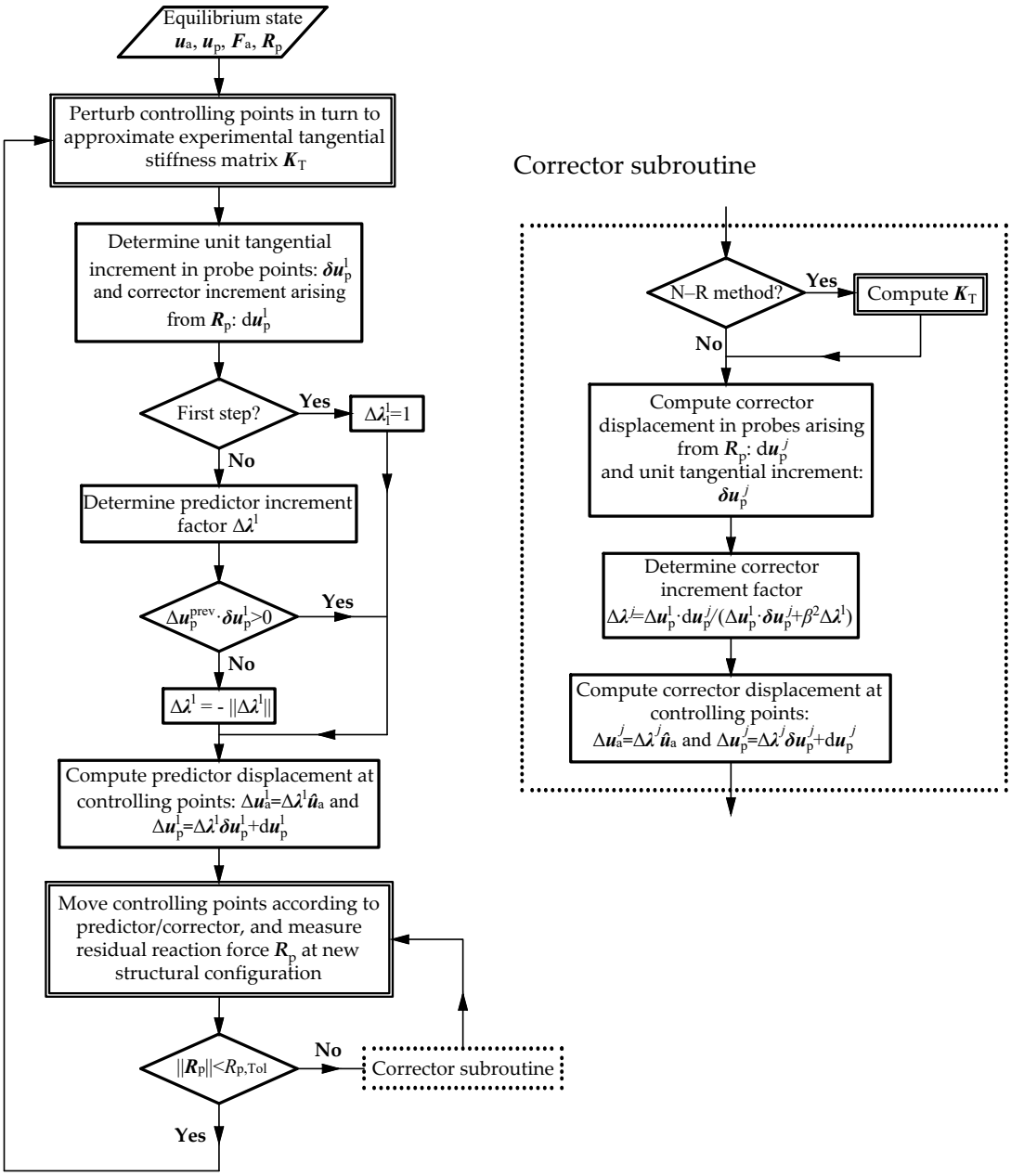

Figure Appendix A.1: Control algorithm for experimental path following. Note that the double-line rectangles represent a *loading* process of the tested structure.

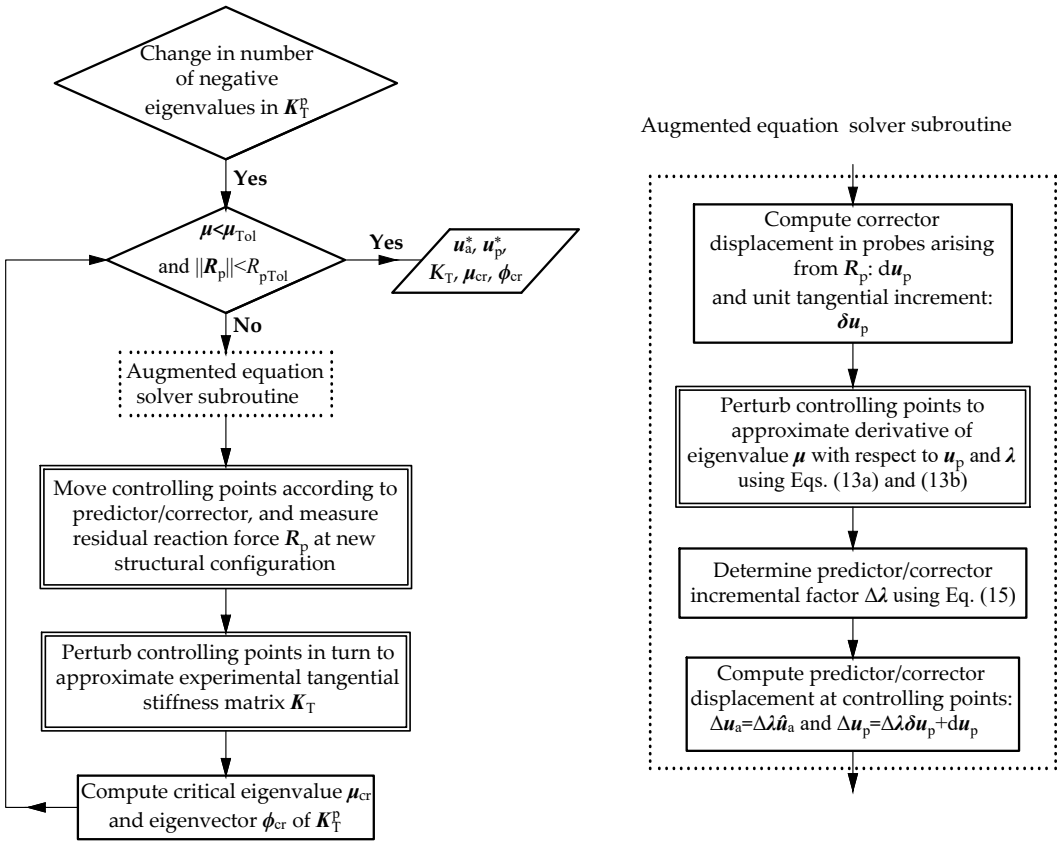

Figure Appendix A.2: Control algorithm for pinpointing critical points; the details are as described in Figure Appendix A.1.

[22] R. Groh, D. Avitabile, A. Pirrera, Generalised path-following for well-behaved nonlinear structures, Comput. Meth. Appl. Mech. Eng. 331 (2018) 394–426.
[23] J. Shen, R. M. J. Groh, M. Schenk, A. Pirrera, Experimental Path-Following of Equilibria Using Newton's Method. Part II: Applications and Outlook, Int. J. Solids Struct. 213 (2021) 25–40.
[24] F. Royer, S. Pellegrino, Buckling of ultralight ladder-type coilable space structures, in: AIAA Scitech 2020 Forum, 2020, p. 1437.
[25] J. Shi, Computing critical points and secondary paths in nonlinear structural stability analysis by the finite element method, Comput. Struct. 58 (1) (1996) 203–220.
[26] ABAQUS, Version 6.14, Dassault Systèmes, Providence RI, USA, 2014.
[27] P. Li, X. Liu, C. Zhang, Interactive buckling of cable-stiffened steel columns with pin-connected crossarms, J. Constr. Steel. Res. 146 (2018) 97–108.
[28] E. Riks, C. C. Rankin, F. A. Brogan, On the solution of mode jumping phenomena in thin-walled shell structures, Comput. Meth. Appl. Mech. Eng. 136 (1–2) (1996) 59–92.
[29] P. R. Everall, G. W. Hunt, Mode jumping in the buckling of struts and plates: a comparative study, Int. J. Nonlin. Mech. 35 (6) (2000) 1067–1079.
[30] J. Singer, J. Arbocz, T. Weller, Buckling experiments: Experimental Methods in Buckling of Thin-Walled Structures, Vol. Volume 1: Basic Concepts, Columns, Beams and Plates, John Wiley & Sons, Inc., 2002.
[31] B. Cox, R. Groh, D. Avitabile, A. Pirrera, Modal nudging in nonlinear elasticity: Tailoring the elastic post-buckling behaviour of engineering structures, J. Mech. Phys. Solids. 116 (2018) 135–149.